Cancer Cell

Article

Multi-omic profiling of follicular lymphoma reveals changes in tissue architecture and enhanced stromal remodeling in high-risk patients

Graphical abstract

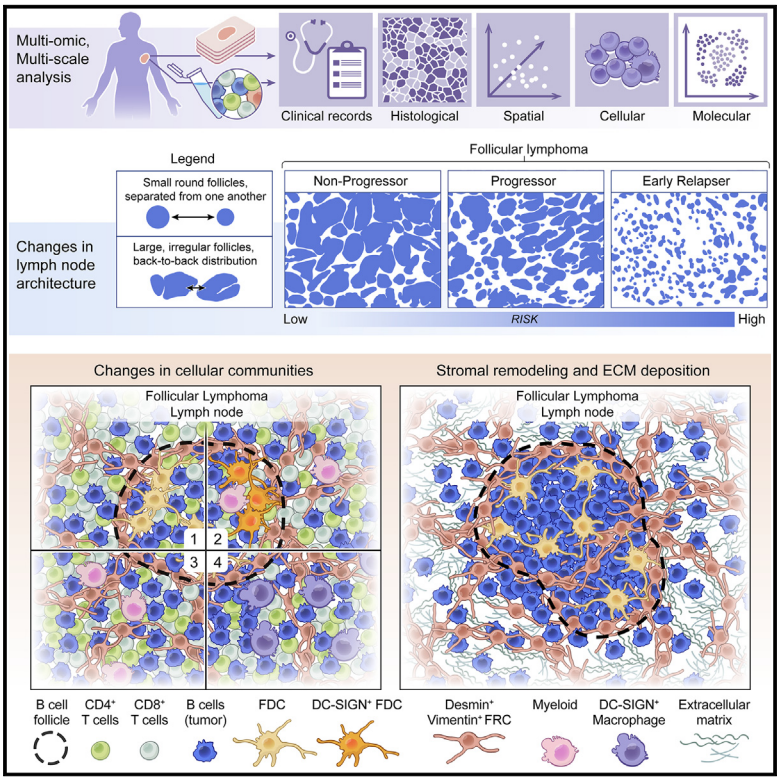

Highlights

- Tumor cells in high-risk FL patients exhibit enhanced B cell receptor signaling
- Distinct follicular growth patterns observed in patients 20 months before relapse
- Enhanced stromal remodeling and ECM deposition in aggressive clinical cases

Authors

Andrea J. Radtke, Ekaterina Postovalova, Arina Varlamova, ..., Louis M. Staudt, Mark Roschewski, Ronald N. Germain

Correspondence

andrea.radtke@nih.gov

In brief

Radtke et al. present a multi-omic survey of the follicular lymphoma tumor microenvironment using advanced sequencing and imaging technologies. Data integration reveals tumor-specific features and microenvironmental patterns in individuals who experience early relapse, the most high-risk patients. These patterns include changes in tissue architecture and enhanced stromal remodeling.

Radtke et al., 2024, Cancer Cell *42*, 444–463
March 11, 2024 Published by Elsevier Inc.
https://doi.org/10.1016/j.ccell.2024.02.001

CellPress

CellPress

Cancer Cell

Article

Multi-omic profiling of follicular lymphoma reveals changes in tissue architecture and enhanced stromal remodeling in high-risk patients

Andrea J. Radtke,[1,13,14,*] Ekaterina Postovalova,[2,13] Arina Varlamova,[2] Alexander Bagaev,[2] Maria Sorokina,[2] Olga Kudryashova,[2] Mark Meerson,[2] Margarita Polyakova,[2] Ilia Galkin,[2] Viktor Svekolkin,[2] Sergey Isaev,[2] Daniil Wiebe,[2] Anna Sharun,[2] Alexander Sarachakov,[2] Grigory Perelman,[2] Yaroslav Lozinsky,[2] Ziv Yaniv,[3] Bradley C. Lowekamp,[3] Emily Speranza,[1,4] Li Yao,[5] Stefania Pittaluga,[6] Arthur L. Shaffer III,[7,8] Danny Jonigk,[9,10] James D. Phelan,[7] Theresa Davies-Hill,[6] Da Wei Huang,[7] Pavel Ovcharov,[2] Krystle Nomie,[2] Ekaterina Nuzhdina,[2] Nikita Kotlov,[2] Ravshan Ataullakhanov,[2] Nathan Fowler,[2] Michael Kelly,[11] Jagan Muppidi,[7] Jeremy L. Davis,[12] Jonathan M. Hernandez,[12] Wyndham H. Wilson,[7] Elaine S. Jaffe,[6] Louis M. Staudt,[7] Mark Roschewski,[7,13] and Ronald N. Germain[1,13]

[1]Lymphocyte Biology Section and Center for Advanced Tissue Imaging, Laboratory of Immune System Biology, NIAID, NIH, Bethesda, MD 20892, USA
[2]BostonGene, Waltham, MA 02453, USA
[3]Bioinformatics and Computational Bioscience Branch, NIAID, NIH, Bethesda, MD 20892, USA
[4]Florida Research and Innovation Center, Cleveland Clinic Lerner Research Institute, Port Saint Lucie, FL 34987, USA
[5]Li Yao Visuals, Rockville, MD 20855, USA
[6]Laboratory of Pathology, NCI, NIH, Bethesda, MD 20892, USA
[7]Lymphoid Malignancies Branch, NCI, NIH, Bethesda, MD 20892, USA
[8]Tumor Targeted Delivery, Heme Malignancy Target Discovery Group, AstraZeneca, Gaithersburg, MD 20878, USA
[9]Institute of Pathology, Aachen Medical University, RWTH Aachen, 52074 Aachen, Germany
[10]German Center for Lung Research (DZL), Biomedical Research in Endstage and Obstructive Lung Disease Hannover (BREATH), 30625 Hannover, Germany
[11]CCR Single Analysis Facility, Cancer Research Technology Program, Frederick National Laboratory for Cancer Research, Bethesda, MD 20892, USA
[12]Surgical Oncology Program, Metastasis Biology Section, Center for Cancer Research, National Cancer Institute, NIH, Bethesda, MD 20892, USA
[13]These authors contributed equally
[14]Lead contact
*Correspondence: andrea.radtke@nih.gov
https://doi.org/10.1016/j.ccell.2024.02.001

SUMMARY

Follicular lymphoma (FL) is a generally incurable malignancy that evolves from developmentally blocked germinal center (GC) B cells. To promote survival and immune escape, tumor B cells undergo significant genetic changes and extensively remodel the lymphoid microenvironment. Dynamic interactions between tumor B cells and the tumor microenvironment (TME) are hypothesized to contribute to the broad spectrum of clinical behaviors observed among FL patients. Despite the urgent need, existing clinical tools do not reliably predict disease behavior. Using a multi-modal strategy, we examined cell-intrinsic and -extrinsic factors governing progression and therapeutic outcomes in FL patients enrolled onto a prospective clinical trial. By leveraging the strengths of each platform, we identify several tumor-specific features and microenvironmental patterns enriched in individuals who experience early relapse, the most high-risk FL patients. These features include stromal desmoplasia and changes to the follicular growth pattern present 20 months before first progression and first relapse.

INTRODUCTION

A chief aim of several international consortia is the construction of organ atlases using next-generation sequencing and spatial approaches.[1–4] The cellular and structural diversity of the lymph node (LN), along with its frequent involvement in metastasis and hematological malignancies,[5,6] warrants construction of high-resolution atlases of normal and malignant human LNs. These resources may aid with clinical decision-making by identifying spatial patterns associated with inferior prognosis, stratifying tumor subtypes by risk, and highlighting mechanisms of therapeutic resistance.

Among the primary malignancies of the lymphatic system, follicular lymphoma (FL) is of special interest for multi-omic

examination. FL is a malignancy of germinal center (GC) B cell origin that extensively remodels the normal lymphoid tissue microenvironment. The disease trajectory of FL patients is heterogeneous, with many patients slowly progressing over several years, and a subset of patients experiencing an aggressive clinical course, often involving histologic transformation into diffuse large B cell lymphoma or other high-grade B cell lymphomas.[7–10] In rare instances, spontaneous remission may occur and is thought to require the generation of an antitumor response following immunologic stimuli.[11] Patients who experience progression of disease within 24 months of initial treatment, termed early relapsers, are the subset with the shortest overall survival and are considered the highest risk.[10,12–15] Despite the urgent clinical need, a predictive tool and consensus treatment approach for early relapsers does not exist.[13] Therefore, a greater understanding of the cell-intrinsic and -extrinsic factors governing progression and therapeutic outcomes is needed for risk-adapted management of FL patients.

FL B cells exhibit genomic and epigenomic alterations that enable immune escape, apoptosis resistance, disease progression, and, in certain patients, histologic transformation.[7,9,16,17] The tumor microenvironment (TME) plays an integral role in supporting the survival of malignant cells throughout the course of disease.[18] Importantly, no single approach can describe the cellular composition of normal LNs, nor identify transcriptomic and histological signatures associated with poor survival in FL patients.[19] To overcome these challenges, we employ advanced sequencing and imaging technologies to generate a molecular and spatial atlas of normal and malignant LNs. We extend key spatial findings to a larger, clinically annotated cohort to reveal architectural changes and cellular communities enriched in high-risk FL patients. In summary, our multiscale analysis of normal and malignant human LNs constitutes a valuable resource for discovery and translational research efforts.

RESULTS

Building a cell- and tissue-level atlas using diverse lymphoid tissue sources

To create atlases of normal and FL LNs, we used state-of-the-art sequencing and iterative bleaching extends multiplexity (IBEX) imaging[20,21] (Figure 1). The study examined excisional LN biopsies from an ongoing clinical trial [NCT03190928], mesenteric LNs deemed grossly normal (nLN1-2), and a reactive LN (rLN1). The clinical cohort included FL patients identified as non-progressors at least 2 years from study entry, progressors within 2 years, or early relapsers (*) (Figure 1A, Table S1, and Figure S1). Excisional biopsies from FL patients, taken prior to any therapy, were analyzed using bulk RNA sequencing (RNA-seq), single-cell RNA-seq (scRNA-seq), IBEX imaging, and additionally prepared as formalin-fixed, paraffin embedded (FFPE) samples for routine diagnostic pathology and multiplexed immunofluorescence (MxIF) imaging (Figure 1B). IBEX imaging was performed with the nuclear marker Hoechst and 39 antibodies targeting diverse cell types in regions of interest averaging 4–12 mm^2. This approach revealed unique histological patterns that could be examined in larger regions (~37–115 mm^2) from clinically relevant FFPE samples using key markers identified from the IBEX data (Figures 1C and 1D). Several methods were integrated, resulting in the construction of a molecular and cellular atlas of normal and malignant LNs across scales and modalities (Figure 1E, Table S2). To test the validity of the spatial findings from the discovery cohort, we performed whole slide imaging (~7–180 mm^2) in a larger cohort using the Cell DIVE[22] and our dye inactivation protocol,[20,21] termed Cell DIVE-IBEX here and throughout (Figures 1E, S1, and Table S2).

Genomic and transcriptomic characterization of FL heterogeneity

We first evaluated the genomic and transcriptomic landscapes of tumor B cells with whole-exome sequencing and bulk RNA-seq. In addition to the expected translocations in the gene encoding the anti-apoptotic protein BCL2 (Table S1), diverse genetic lesions were identified in recurrently mutated genes previously associated with FL pathogenesis (Figure 2A).[7] Alterations in chromatin-modifying genes such as *KMT2D*, *EZH2*, *ARID1A*, and *CREBBP*, as well as genes involved in cell migration and immune regulation (*CXCR4*, *TNFRSF14*, *CIITA*),[7] were observed in progressors and non-progressors alike (Figure 2A). The cellular composition of FL samples was next evaluated by a deconvolution algorithm[23] for data derived from bulk RNA-seq (Figure 2B, Tables S3, and S4). B cells were the most abundant cell type, representing more than 60% of deconvolved cells from bulk analysis (Table S2). Myeloid and stromal cells, representing less than 2% of deconvolved cells per sample, were broadly classified as macrophages, monocytes, fibroblasts, and endothelial cells using lineage-specific genes (Tables S2, S3, and S4). In addition to analyzing the cellular composition of FL patient samples, malignant B cell receptor (BCR) sequences were identified from bulk RNA-seq based on the fraction of dominant immunoglobulin (Ig) sequences (Figure 2C).[24] Dominant clones were found in all patients except FL-1, a spontaneous remitter (Table S1). To further evaluate the clonal repertoire of FL B cells and overcome challenges arising from matching heavy and light chains from bulk suspensions, 5′ scRNA-seq was also performed (Figure 2C). The malignant Ig repertoires identified from bulk and scRNA-seq showed a similar monoclonal Ig distribution for all samples except for FL-1, confirming the utility of using bulk RNA-seq to deconstruct B cell clonotypes.

Cellular composition of human LNs using scRNA-seq

To evaluate gene expression profiles at single-cell resolution, we performed scRNA-seq on samples from this same cohort of FL patients. We additionally extended our studies to healthy LNs as a control and potential resource for LN atlas building efforts (Figures 2D–2F, S2A, and Table S2). Lymphoid populations varied in their relative abundance across samples (Figures 2F, S2A, and Table S2). These populations included naive follicular B cells (*MS4A1*, *CD19*, *FCER2*, *SELL*), GC B cells (*CD83*, *GMDS*, *AICDA*, *BCL6*, *CD81*), cycling B cells (*MK167*, *UBE2C*, *CD81*), and tumor B cells (*BCL2*, *MME*, *TCF4*) found only in FL samples (Figures 2E and 2F). Analysis of T cells revealed subpopulations of $CD4^+$ and $CD8^+$ T cells including T regulatory cells (Tregs, *FOXP3*, *CTLA4*, *IKZF2*, *TIGIT*), T follicular helper cells (Tfh, *PDCD1* (PD-1), *ICOS*, *TOX2*, *TIGIT*), and distinct populations of $CD8^+$ T cells expressing several cytotoxic (*GZMA*, *PRF1*, *NKG7*) and exhaustion/activation-related (*LAG3*, *HAVCR2*

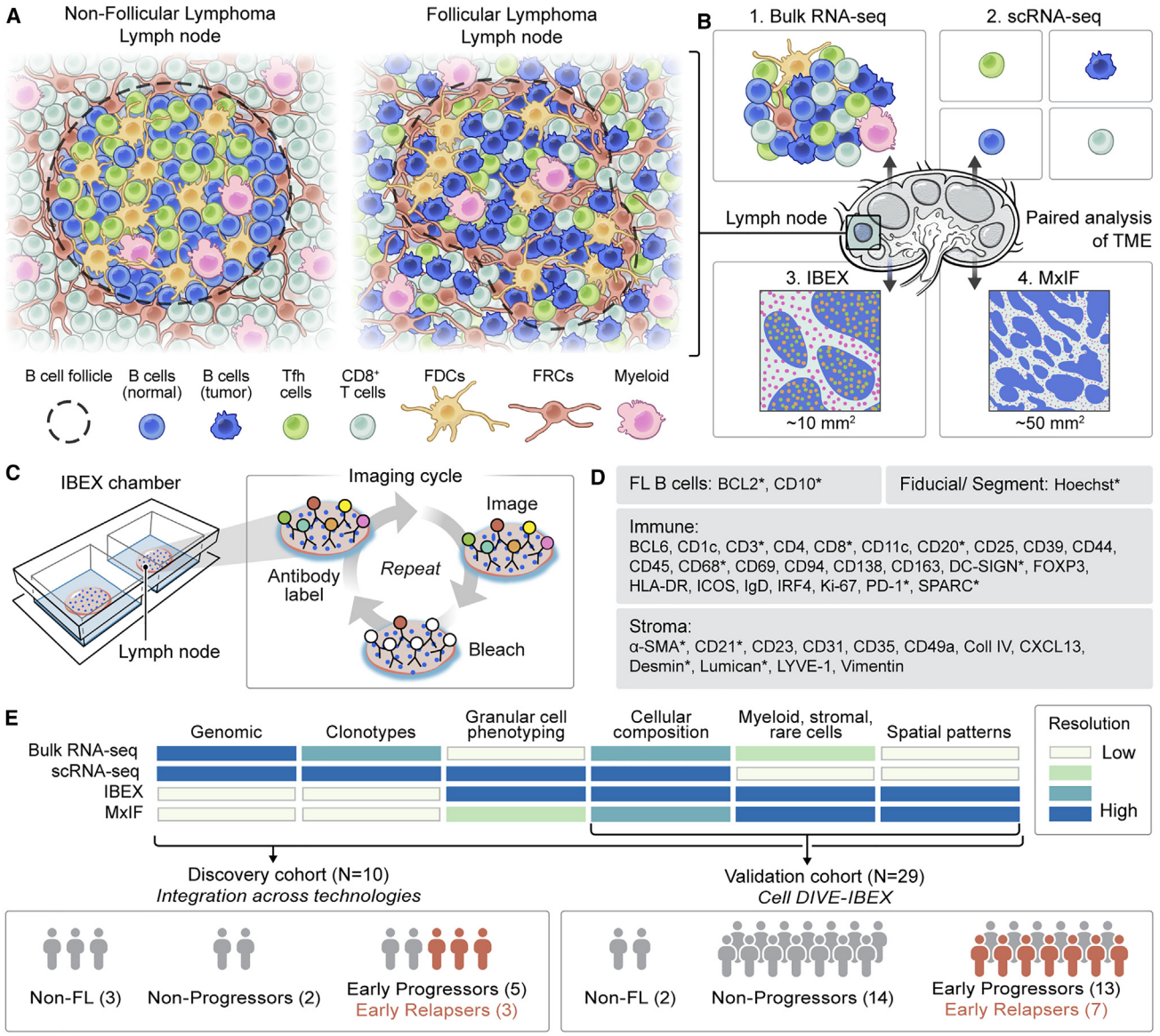

Figure 1. Construction of LN atlases using multiple omics and imaging technologies

(A) Tissues were profiled from non-FL and FL LNs. Schematic shows enlarged and stylized follicles.

(B) Paired samples from normal and FL patients were profiled using multiple assays. Normal LNs were examined only by single-cell technologies (scRNA-seq and IBEX). Tissue microenvironment (TME), multiplex immunofluorescence (MxIF).

(C) Schematic depicting IBEX imaging technique.

(D) Protein biomarkers targeted with IBEX or MxIF (*) grouped by cell type.

(E) Comparison of information provided by each technology for each cohort. Resolution provided as an estimate only and based on analyses described in this work. See also Figure S1, Tables S1, and S2.

(TIM-3), *TIGIT*) markers. These "exhausted CD8$^+$ T cells" were nearly absent from non-FL LNs but enriched in rLN1 and LNs from FL patients, suggesting chronic inflammatory reactions in these tissues (Figure 2F). Evaluation of myeloid and stromal populations by scRNA-seq frequently requires specialized protocols for tissue dissociation and cell enrichment, increasing the risk for altered gene expression profiles.[25] To minimize these artifacts, we performed single-cell analysis on suspensions obtained with limited intervention. Although representing a small fraction of total cells, plasmacytoid dendritic cells (*IRF7*, *ITGAE*, *ITM2C*, *PLAC8*, *TCF4*), macrophages (*C1QA*, *IL1B*, *ITGAX*), cDC1 DCs (*C1orf54*, *CADM1*, *CLNK*), and follicular dendritic cells (FDCs) (*CR2*, *CXCL13*, *FDCSP*) were profiled at varying frequencies across normal and FL samples (Figures 2D–2F, Table S2).

BCR signaling and ECM remodeling pathways are upregulated in early relapsers

We performed gene set enrichment analysis of scRNA-seq populations to identify the biological processes driving early

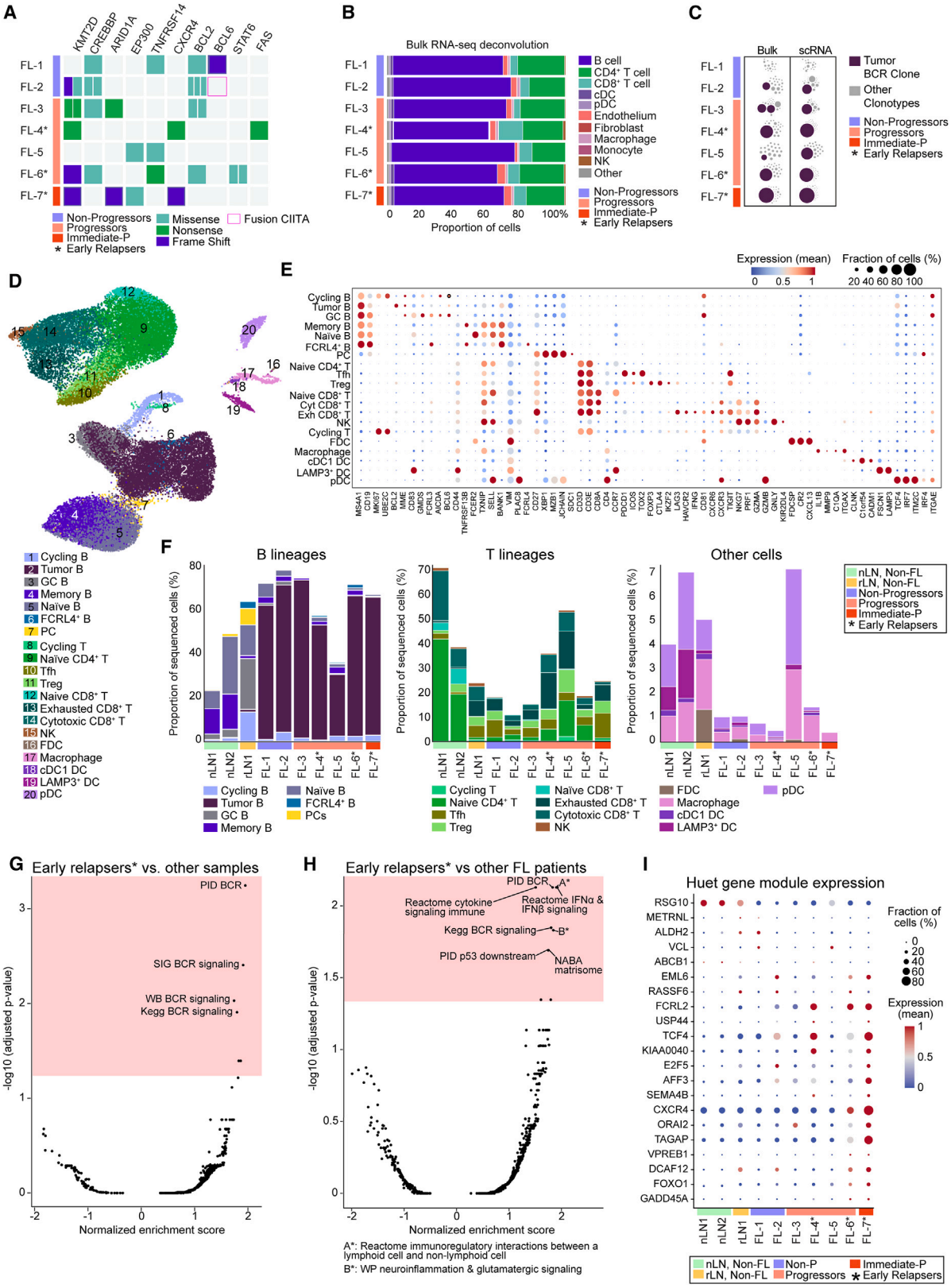

(legend on next page)

progression and relapse in this initial set of FL patients.[26] We explored the gene expression patterns distinguishing B cells in early relapsers from B cells in all other samples. The top pathways upregulated in early relapsers all involved BCR signaling (Figure 2G). Several shared genes were identified as the leading-edge subset, defined as high-scoring genes accounting for the enrichment signal.[26] These included mRNAs encoding for *CD19*, *BLNK*, *SYK*, *and LYN* (Table S2). We next compared the B cells from early relapsers to the B cells from all other FL patients. As before, the B cells from early relapsers upregulated components of BCR signaling pathways along with molecules involved in cytokine signaling, immune activation, and immunoregulation (Figure 2H, Table S2). We additionally observed enrichment of a gene set associated with glutamatergic signaling including transporters (*SLC38A1*, *SLC2A3*, *SLC38A2*, *SLC2A1*) and enzymes (*GLUL*, *GLS*) involved in glucose and glutamine metabolism (Table S2).[27] B cells of early relapsers exhibited high expression of genes involved in extracellular matrix (ECM) remodeling including those encoding growth factors, ADAMs, annexins, and galectins (Figure 2H, Table S2).[28]

In addition to the unbiased approach described previously, we evaluated gene signatures correlated with poor outcome in FL patients[8] as well as IRF4-associated molecular signatures dysregulated in other hematological malignancies[29] (Figures 2I and S2B–S2D). B cells from the early relapsers had elevated levels of transcripts from genes correlated with a high risk of progression (Figure S2B).[8] However, considerable interpatient heterogeneity was observed in the expression of individual genes summarized by the Huet module (Figure 2I). Within the IRF4-associated module, the early relapsers uniformly showed increased expression of *FOXP1* (adjusted p value <0.0001, log fold change = 1.07) (Figure S2C). This transcription factor has been shown to predict adverse failure-free survival in FL patients treated with rituximab and chemotherapy.[30] Of the three early relapsers, FL-4 and FL-7 displayed the highest aggregate expression of IRF4-associated genes (Figure S2D).

We next examined Ig clonotypes in our study using directed amplification and sequencing of BCRs. Retention of surface Ig expression is critical for malignant cells as it provides a mechanism of antigen recognition and survival signaling in the TME. While ~40%–50% of FL B cells are reported to undergo isotype switching to IgG, IgM is frequently observed in early stages of FL and thought to favor GC reentry.[31] The majority of progressors expressed IgM heavy chains except for FL-5, whose tumor cells had class switched to IgG (Figure S2E). In summary, bulk and scRNA-seq revealed diverse cell-intrinsic factors governing survival and progression in FL patients.

Quantification of diverse cell types at single-cell and spatial resolution using IBEX

To provide a spatial context for the cellular heterogeneity observed across normal and FL LNs, we performed 40-plex IBEX imaging on tissue samples from this initial cohort (Figure 3A). For accurate quantification of cell types *in situ*, individual cells were segmented using several membrane markers and a deep-learning-based approach (Figures S3A–S3D, Table S5, STAR methods). Using this approach, 37 phenotype clusters were identified, resulting in a single-cell proteomic dataset of 1.8×10^6 cells (Figure 3B, Table S2). Phenotype clusters were annotated into cell types based on protein biomarker expression, visualized using the data dimensionality reduction method uniform manifold approximation and projection (UMAP), and named according to their dominant marker expression and, whenever possible, relevant cell ontologies[5,32] (Figure 3C). IBEX imaging revealed a diversity of B and T cell populations across FL samples (Figures 3A–3E, S4A, S4B, and Table S2). Although myeloid and stromal cell populations were identified using the segmentation approaches outlined here (Figures 3B and 3C), these cell types pose significant challenges due to their complex morphology.[33,34] To overcome these challenges, we developed a method for profiling myeloid and stromal cells based on the creation of image masks that use pixel-level data instead of discrete segmented cells (Figure S3D). Cell quantification of myeloid and stromal lineages was performed using the indicated markers and normalized across samples by area imaged (Figures 3F–3I, Table S2). Using this approach, we evaluated the location and relative abundance of blood endothelial cells, lymphatic endothelial cells, FDCs, and CD49a$^+$ cytokine/chemokine-producing fibroblastic reticular cells (FRCs) previously identified in FL LNs[35] (Figures 3F–3I and S4C). Quantitative imaging revealed these cell types to be far more abundant than appreciated by methods employing routine tissue dissociation approaches (Figures 3G–3I, Table S2). The resulting data underscore the importance of studying complex cell types in intact tissues.

Distinct histological patterns identified in high-risk FL patients

Previous studies have linked clinical progression to the distribution of cell types inside and outside of B cell follicles.[36,37] B cell

Figure 2. Cellular composition and gene expression patterns of normal and FL samples

(A) Genomic alteration landscape. Each line provides the detected mutations and fusions (cyan - missense mutation, green - nonsense mutation, violet - frameshift mutation, pink box - fusions) patients annotated based on progression status.

(B) Cell composition reconstruction from bulk RNA-seq data.

(C) BCR calling from RNA-seq. Bubble corresponds to a unique or group of similar CDR3 sequences from heavy immunoglobulin genes. Size of circle corresponds to clonotype abundance. Bulk RNA-seq (bulk), scRNA-seq (scRNA) here and throughout.

(D) UMAP plot of 36,212 single cells from all samples.

(E) Expression of selected markers used for cell annotation of scRNA-seq clusters. Plasma cells (PCs), pDCs, exhausted (Ex), and cytotoxic (Cyt).

(F) scRNA-seq frequencies of indicated cell types from each patient.

(G) Gene set enrichment analysis of B cells from early relapsers (*) compared to all other samples plotted as enrichment score on the x axis compared to the -log10 of the adjusted p value on the y axis. The pink box shows a cutoff of adjusted p value <0.05 calculated using mSigDB (described in STAR methods). Each point represents a gene set, with top scoring gene sets labeled.

(H) Same as G but only comparing B cells from early relapsers to other FL samples.

(I) Dynamic expression of individual genes associated with Huet gene signature. See also Figure S2, Tables S1–S3, and S4.

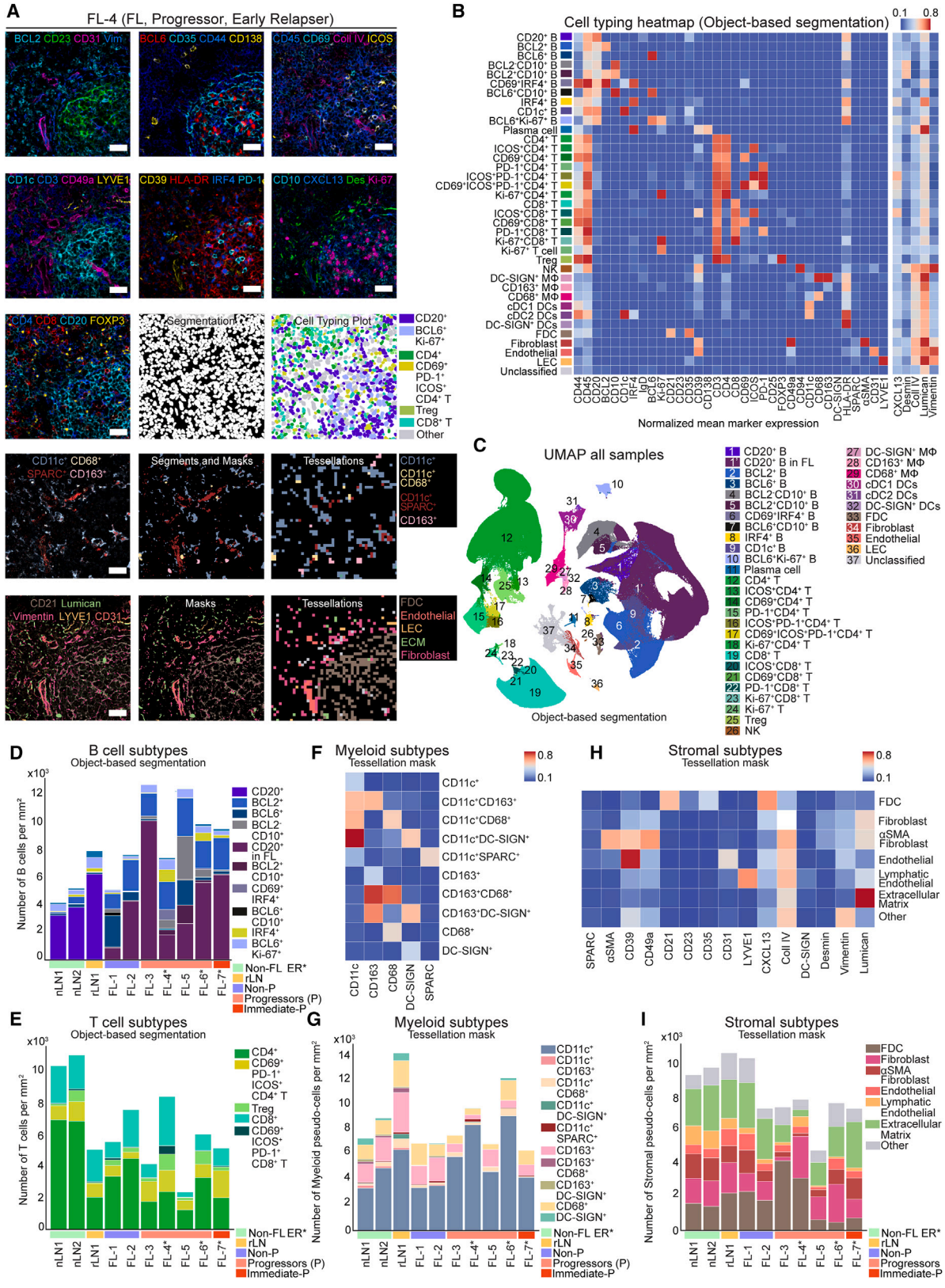

(legend on next page)

follicles varied in number and size and were identified as CD20$^+$CD21$^+$ structures (Figure S5A). Further analysis revealed differences in the presence of CD8$^+$ T cells, tingible body macrophages (CD11c$^+$SPARC$^+$, CD11c$^+$CD68$^+$), and FDCs (combinations of CD21$^+$CD23$^+$CD35$^+$) in the neoplastic follicles of FL LNs (Figures 4A and 4B). In agreement with the literature,[5,38] the secondary follicles of non-FL LNs were enriched for GC (BCL6$^+$Ki-67$^+$) B cells, T follicular helper (Tfh: CD3$^+$CD4$^+$CD69$^+$ PD-1$^+$ICOS$^+$), and tingible body macrophages (Figure 4B). The early relapsers had several distinguishing patterns (Figure S5B) including the expansion of desmin$^+$ fibroblasts around and within B cell follicles (Figure 4C). While less abundant than other myeloid and stromal cells (Figure 4B), increased proportions of DC-SIGN$^+$ cell subtypes were found in the follicles of early relapsers (Figure S5B), providing a potential pro-survival signal for malignant B cells via engagement with glycosylated BCRs.[31,39,40] In contrast, DC-SIGN is traditionally found on CD163$^+$ macrophages in the medulla and subcapsular sinus but absent from the secondary follicles of normal LNs (Figures S5B and 4C). IRF4$^+$ tumor B cells, previously implicated in aggressive FL cases with poor overall survival,[41] were identified in direct contact with DC-SIGN$^+$ cells, Tfh cells, and cells expressing vimentin, a recognized autoantigen in FL[42] (Figure S5C). These findings are concordant with previous data demonstrating that IRF4 is upregulated in B cells following BCR engagement and/or T cell co-stimulation.[43] The histological patterns identified in all three early relapsers—desmin$^+$ FRC expansion around B cell follicles and DC-SIGN$^+$ cells within follicles—were beginning to emerge in a non-progressor (FL-2) before therapy (Figure 4C). Interestingly, our scRNA-seq analyses revealed higher expression of the Huet gene module in this patient than in other early progressors (Figures 2I and S2B). In summary, IBEX revealed changes to the myeloid and stromal components of the TME with diagnostic and predictive potential.

LN cellular composition is dramatically altered in malignancy

We evaluated the cellular ecosystems present in IBEX images using a graph neural network-encoding approach and K-Means clustering to identify individual neighborhoods encompassing similar cell types and distributions.[44] Cell-cell interactions were visualized on a schematic interaction graph that included 8 cell types identified by object-based segmentation, 13 stromal masks, and 5 myeloid masks using the indicated markers (Figures 5A and 5B). Selected cell types covered major lineages identified by IBEX and scRNA-seq analysis. The resulting approach yielded 15 neighborhoods named for the dominant cell type within each community: (Figures 5A, 5B, and Table S2). Our workflow classified the well-defined anatomical structures of non-FL LNs into discrete communities, e.g., GC (B1) and mantle zone (B2) (Figure 5C, Table S2). In contrast, FL LNs lacked the hallmark structures of normal LNs (Figures 5D, 5E, S5D, and S5E). B cell-enriched clusters (B1-B2) were predominantly located inside the follicles of non-FL LNs (Figures 5F, S5D, and S5E). All other B cell-enriched clusters were distributed both within and outside of the follicles (B3-B5) with B3 and B4 largely absent from non-FL LNs and expanded in certain progressors (Figures 5E, S5D, and S5E). The majority of T cell-enriched communities were located in the intrafollicular cortex and/or paracortex (T2-T6); however, one community (T1) was found inside the follicles of FL and non-FL LNs alike (Figures S5D–S5E). The remaining communities were myeloid (M1-M2) and stromal (S1-S2)-enriched clusters corresponding to anatomical structures such as medullary and paracortical sinuses (Figures 5E, 5F, and Table S2). The community composition of secondary and neoplastic follicles was heterogeneous across non-FL and FL samples, respectively (Figure 5G). However, individual follicles were more similar within samples than between samples (Figures 5G and 5H). Thus, advanced image analysis identified cellular communities present in normal LNs that are altered in malignancy.

Spatial patterns are preserved across imaging modalities

We extended our studies to larger tissue sections using key markers of interest. Multiplexed imaging panels, designed based on IBEX data, were applied to serial sections from FFPE samples (Table S6). Following image acquisition, the conservation of histopathological patterns between IBEX small region of interests (ROIs) and MxIF large ROIs was evaluated (Table S2). Samples identified to have abundant populations of follicular CD8$^+$ T cells and DC-SIGN$^+$ FDCs by IBEX imaging were confirmed to have these unique cell types by MxIF (Figure 6A). The presence of desmin$^+$ stromal cells around the follicles of early relapsers and a non-progressor was additionally confirmed in FFPE tissue sections with different antibody clones (Figure 6B). We next investigated whether follicle shape and size could determine whether the ROI selected for IBEX imaging captured the larger FL sample (Figure S6A). For quantitative assessment between samples, follicle masks were obtained through manual annotation by pathologists using CD20 and CD21 signals (Figure S5A). Using an agglomerative clustering approach, follicles

Figure 3. Spatial survey of complex tissues using IBEX

(A) Representative IBEX images of selected markers, scale bar 30 μm. Vimentin (Vim), Desmin (Des), Collagen IV (Coll IV). Row 3: Cell segmentation and cell typing plots for the same region. IBEX images of myeloid (Row 4) or stromal (Row 5) markers (left), segments and masks of immunofluorescence (IF) signal (middle), and tessellation masks of populations (right).

(B) Heatmap of normalized mean marker expression used to define cell populations. 37 clusters were identified using cell segmentation.

(C) UMAP plot of 0.9 × 10^6 cells from all samples, colored by cell populations identified by IBEX. Quantification of B.

(D–E) Quantification of B cell (D) or T cell (E) subpopulations obtained from IBEX and normalized by area imaged per sample.

(F) Heatmap of the normalized mean marker expression of biomarkers for myeloid cell phenotyping by tessellation masks.

(G) Quantification of myeloid subpopulations obtained from IBEX where cells are expressed as tessellation square counts per sample.

(H) Heatmap of the normalized mean marker expression of biomarkers for stromal cell phenotyping by tessellation masks.

(I) Quantification of stromal subpopulations obtained from IBEX where cells are expressed as tessellation square counts per sample. See Figures S3, S4, Tables S2, and S5.

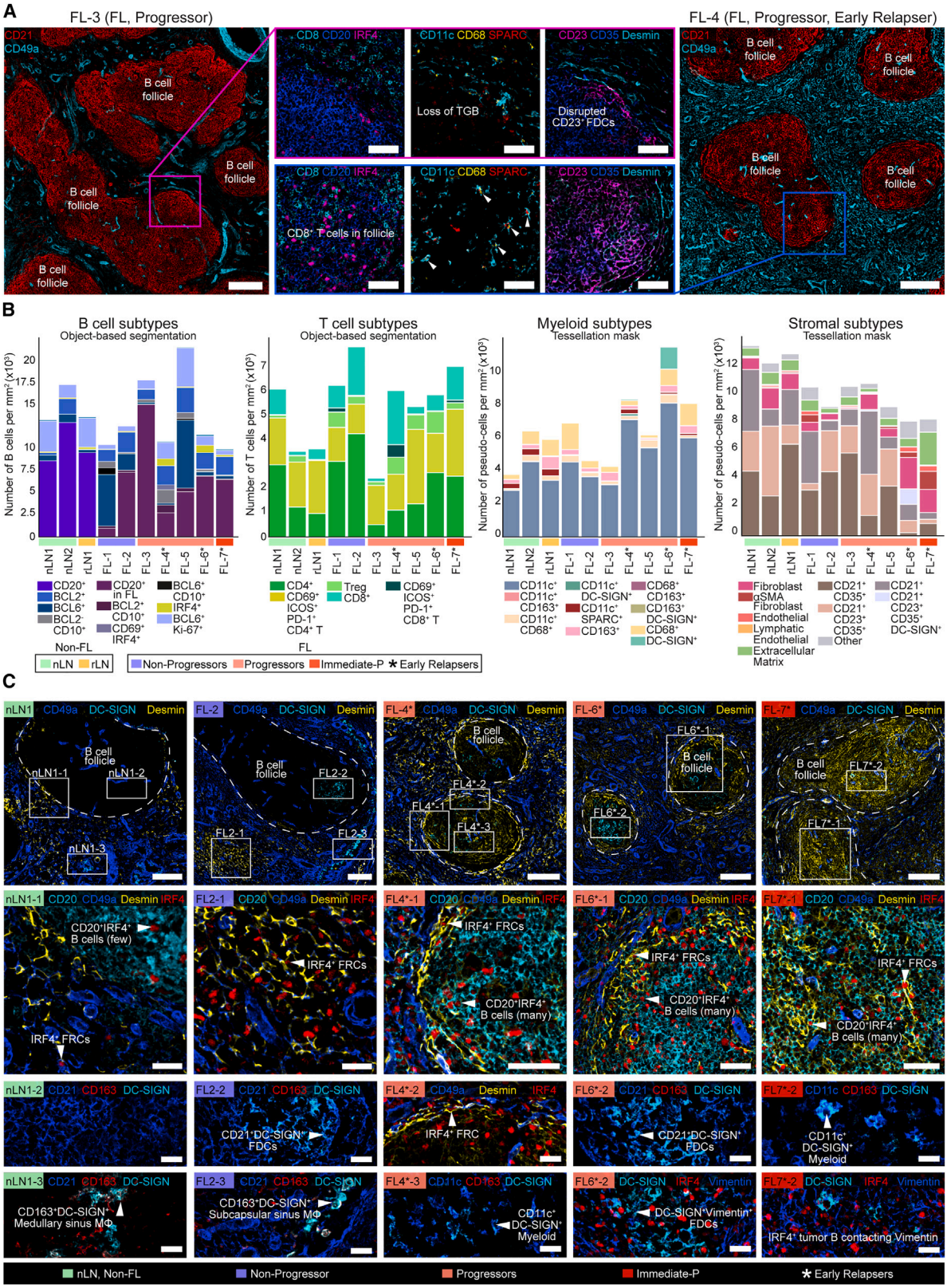

(legend on next page)

were subdivided into 7 subtypes and their distribution was compared between IBEX and MxIF images (Figures 6C and 6D). In general, IBEX and MxIF images derived from the same donor had follicles of similar shape and size (Figure 6E).

Having observed concordance between the follicular composition of small IBEX ROIs and larger FFPE ROIs (Figure 6E), we evaluated the community composition of these tissues using a similar approach to the one outlined in Figure 5 (Figures S6B and S6C). Cellular communities were defined based on 11 common markers corresponding to major cell lineages and key anatomical structures. As a result, 13 community clusters were obtained using both IBEX and MxIF data (Figures 6F and 6G). Our community-level analysis provided a qualitative and quantitative means for assessing similarities across samples and imaging modalities (Figures 6H and 6I). Both IBEX and MxIF images of two early relapsers (FL-6, FL-7) exhibited reduced T cell-enriched communities (T1, T2) and increased proportions of B cells in contact with $CD4^+$ T cells (B1) (Figure 6H). To provide a metric for estimating the area of tissue to image for accurate sampling, we evaluated the mean tessellation correlation based on different sized ROIs (Figures 6J and S6D). The obtained correlations were greater than 0.8, suggesting that IBEX ROIs are fairly representative of whole tissue sections.

Myeloid and stromal cell undersampling revealed by data integration

To create a reference atlas based on data collected from samples derived from this initial cohort, we followed several paths to capitalize on the strengths of each technology while overcoming platform-specific limitations. We compared the relative abundance of major cell populations identified by bulk RNA-seq through cell deconvolution, scRNA-seq cell typing, and IBEX image analysis using cell segmentation and masks (Figure 7A). In general, similar proportions of major lymphocyte populations were observed across technologies (Figure 7A). However, myeloid and stromal cell populations were significantly underrepresented in RNA-seq datasets generated without specialized tissue dissociation methods or cell enrichment (Figure 7A, Table S7). On average, IBEX images had 36 times more cells than paired scRNA-seq datasets (Table S2), empowering the study of rare cells that may require analysis of tens of thousands of cells via scRNA-seq (Figure 7B).

As cytokines and chemokines are essential for normal tissue organization and malignancy-induced remodeling,[45] we next evaluated correlations between gene signatures curated from bulk RNA-seq with cellular communities derived from IBEX images (Figures 7C, 7D, Tables S8, S7A, and S7B). Given gene- and protein-level evidence for ECM remodeling among early relapsers (Figures 2H and 4C), we explored gene signatures associated with fibrosis, including matrix metalloproteinases, collagen deposition, and (myo)fibroblasts (Figures 7C and S7A). The T2 community, rich in FRCs expressing CD49a (*ITGA5*) and desmin (*Des*) (Figure S7A), was primarily found in the paracortex of non-FL LNs and the follicles of two early relapsers. The T1 community was correlated with gene signatures associated with B cell antibody production, Th2 immunity, and T cell exhaustion (Figures 7C, 7D, and Table S8).

Bulk RNA-seq identified cytokines strongly correlated with IBEX communities, including the major pro-fibrotic factor TGF-β and its isoforms (Figures S7A and S7B).[46,47] Several chemokines (CCL4, CCL5, CXCL13) involved in the recruitment of diverse cell types to the TME were also found (Table S8). Our scRNA-seq analysis revealed elevated CCL4 and the CXCL13-CXCR5 gene pair in FL B cells from two early relapsers (FL-4, FL-7) (Figures 7E–7G). $LAG3^+$ $CD8^+$ T cells, present only in rLN1 and FL LNs (Figure 2F), showed elevated levels of CCL4-CCR5, CCL5-CCR5, and CXCL13-CXCR5 gene pairs (Figures 7E–7G). Increased numbers of $CD8^+$ T cells infiltrated the follicles of two early relapsers (FL-4, FL-7, Figures 4A, 4B, and 6A), suggesting a potential mechanism involving tumor B cell recruitment of $CD8^+$ T cells through the secretion of CCL4 and other soluble factors. We used IBEX imaging to confirm the presence of $CXCL13^+$ FL B cells[48] and expansion of $CXCL13^+$ FDCs and $CD49a^+$ FRCs in FL patients[35] (Figure 7H). Lastly, dense networks of $lumican^+$ fibers were found around the follicles of early relapsers (Figures 7I and S7C).

High-risk patients are distinguished by architectural changes and enhanced stromal remodeling

To examine whether our spatial findings could be extended to a larger patient cohort, we performed whole slide imaging of FFPE specimens using the Cell DIVE-IBEX method (Figures 1E, S1, Table S1, Figures 8, and S8). Due to technical constraints related to antibody panel design,[49,50] an 11-plex immune panel and 6-plex stromal panel were applied to serial sections (Tables S2, S6, Figure S8C–S8E). We extended our quantitative follicle analysis from 1,041 follicles (Figures 6 and S6) to 4,681 follicles, revealing 5 clusters defined by 6 parameters related to the size, shape, and distribution of follicles (Figures 8A–8D, S8A, and S8B). Follicles were quantified in all samples except for FL-13 which had no discernable follicles (Figure S8A). In general, non-progressors and early progressors exhibited a more back-to-back distribution of follicles characterized by a reduction in the minimum distance between neighboring follicles. Although a morphological continuum was observed, neoplastic follicles in early relapsers tended to be smaller, irregularly shaped, and separated by greater distances, e.g., follicle type 4 (Figure 8D). One progressor, FL-5, relapsed at 30 months and therefore did not meet the clinical criteria of an early relapser (<24 months). However, differences in follicle composition were observed when FL-5 was analyzed with samples from patients experiencing early relapse versus progressors who did not relapse (Figure 8D). It is worth emphasizing that these histological patterns were present at the time of biopsy an average of 20 months before first progression and first relapse in an untreated patient cohort (Figures 8E and S1).

Figure 4. Cellular composition and histological patterns of secondary and neoplastic follicles

(A) IBEX images depicting differences in the shape and cellular composition of B cell follicles from FL patients, scale bars 200 μm or 50 μm (blue and magenta insets). Tingible body macrophages (TGB, arrowheads).

(B) Quantification of major B, T, myeloid, and stromal cells found within B cell follicles, obtained from IBEX and normalized by area imaged per sample.

(C) IBEX images depicting histological patterns shared among early relapsers. Scale bar is 100 μm, 50 μm (Inset 1), and 25 μm (Insets 2 and 3). See also Figure S5.

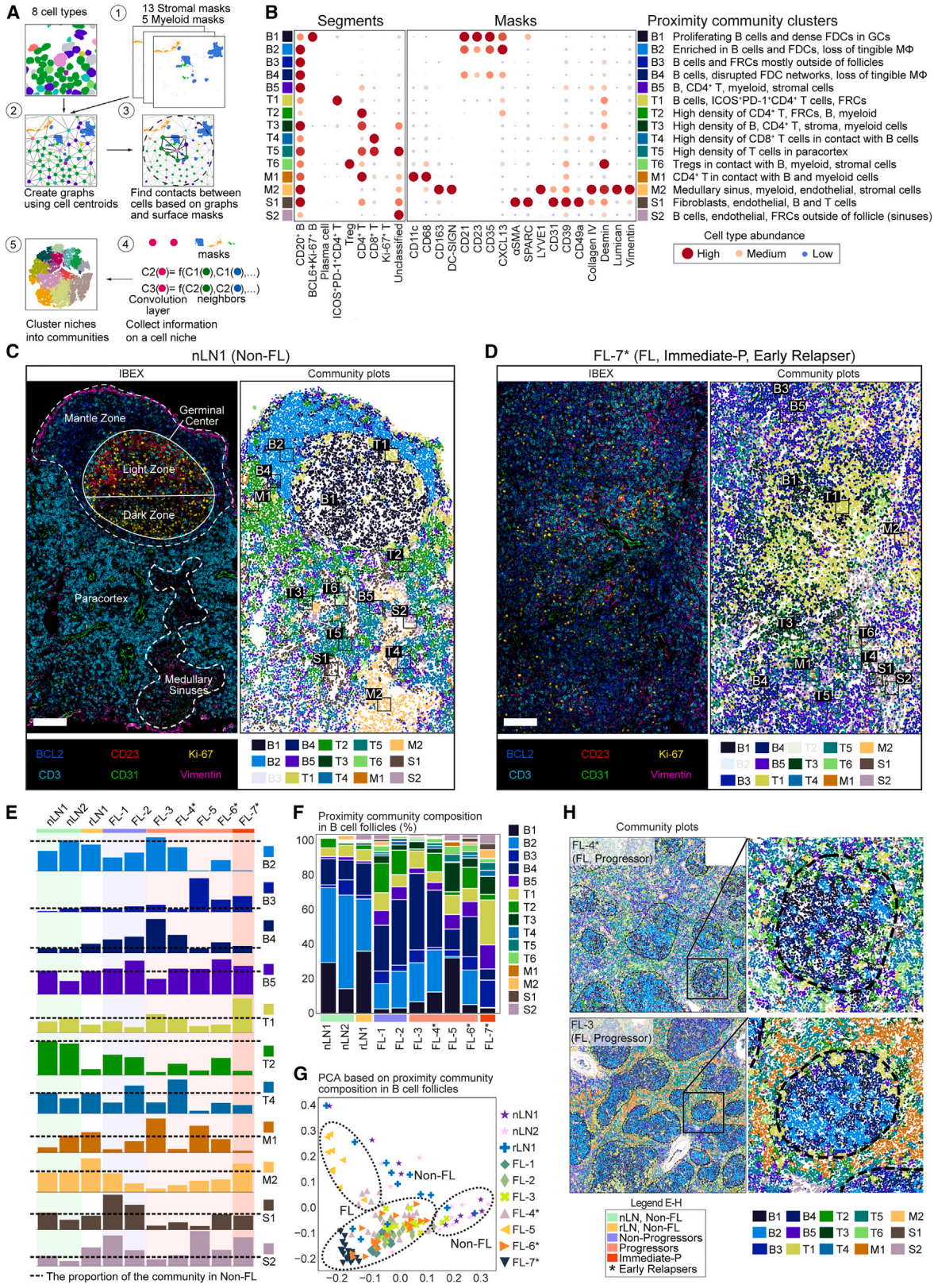

(legend on next page)

In addition to quantifying architectural changes in the FL TME, we applied the tessellation community workflows described earlier to Cell DIVE-IBEX images (Figures 8F–8M, Table S2). The B1 community, comprised of tumor B cells and FDC networks, was found in all FL samples but progressively declined in progressors and early relapsers (Figure S8F). As before, we observed DC-SIGN$^+$ FDC networks in a subset of FL patients and this was captured by the B2 community consisting of tumor B cells in well-defined follicles with FDC networks (Figure S8G). Importantly, not all FDC networks in a single tissue section were DC-SIGN$^+$ (Figure S8C) and this heterogeneity, coupled with the large area imaged, likely contributes to the low frequency of this community. Contacts between CD68$^+$ macrophages and tumor B cells were captured by the M1 and M2 communities with a slight increase in the DC-SIGN$^+$ macrophage community (M1) in the early relapsers (Figures 8H and 8I). The community with the highest expression of IRF4$^+$ tumor B cells, T2, varied among FL patients but was elevated in FL-6 and FL-7, two early relapsers that were shared between the discovery and validation cohorts (Figure S8H). The appearance of a community negative for all markers (S1) (Figure S8D) prompted investigation into the stromal composition of the FL TME. We validated a loss of B cell communities with minimal stromal involvement (B1), and a corresponding increase in cellular communities comprised of B cells, fibroblasts, and ECM (S3) distributed across whole tissue sections (Figures 8K–8M).

Regardless of the clinical group, considerable heterogeneity was observed in the cellular composition of each sample. This phenomenon effectively masked the significance of individual communities and failed to identify key cell types defined by the immune and stromal panels (Figures S8I, S8J, and Table S2). To identify major drivers of early relapse, we constructed a linear model using every combination of the 16 communities (Figures 8N–8P, STAR methods). The most significant model to distinguish early relapsers from other FL patients included three stromal communities (S1, S4, and S3) enriched for desmin$^+$vimentin$^+$ fibroblasts and ECM-associated proteins including lumican and secreted protein acidic and rich in cysteine (SPARC), a protein expressed by macrophages, endothelial cells, and stromal cells involved in cell-matrix interactions.[51] Immune communities enriched for macrophages, including DC-SIGN$^+$ subsets, were the next most abundant communities present in significant models (Figure 8O). However, S1 and S4 communities were key drivers in identifying early relapsers as these patients were either high for the S1 or S4 communities (Figure 8P), raising the possibility of two distinct mechanisms of relapse in these patients. Potential mechanisms to investigate further include, but are not limited to, the fibroproliferative potential of FRCs and their contribution to ECM organization and therapy resistance.

DISCUSSION

Ambitious efforts by international consortia have highlighted the importance of tissue atlases for discovery efforts and translational research.[1–4,52] Accordingly, the multimodal approach we describe here yielded several insights and technical advances. One key finding is the identification of several distinguishing features in the TMEs of high-risk FL patients. The malignant B cells of early relapsers exhibited several characteristics consistent with antigen engagement within the TME. The histological patterns we identified in the discovery cohort were confirmed in additional clinically relevant FFPE samples using targeted imaging of key immune and stromal markers. There was a reduction in follicle size and an increase in the distance between neighboring follicles at the time of biopsy, an average of 20 months before relapse. Based on the community analysis performed in parallel, we hypothesize that these architectural changes are due to a loss of FDC networks and progressive expansion of stromal cells within and around the follicles of high-risk FL patients. Together, this work suggests that antibodies directed against desmin, vimentin, and lumican may warrant inclusion in established diagnostic panels for risk-adapted management of FL patients. To this end, immunohistochemical evaluation of intratumoral vimentin was identified to predict histologic transformation in FL patients,[53] and a scRNA-seq study demonstrated the upregulation of transcripts involved in ECM remodeling in FL stromal cells.[54]

Bulk RNA-seq has provided insight into the mutational burden, copy number alterations, and cellular composition of various tumors.[4] The cost-effectiveness of bulk RNA-seq, in combination with previously reported mutations and disease-associated gene expression signatures, makes this an attractive approach for stratifying patients for personalized treatment options. Here, we extend the utility of bulk analysis by correlating gene signatures associated with cell types and states to cellular communities found *in situ*. Despite these advances, our results demonstrate that bulk RNA-seq does not allow for molecular dissection of rare subpopulations of cells.[4,55]

Our scRNA-seq studies revealed 20 cell types with dominant B cell clones emerging in clinical cases associated with early progression and relapse after therapy. Others have speculated on the critical role for antigen selection in the clonal evolution

Figure 5. Cellular communities are shared across normal LNs but distinct in tumors

(A) Proximity community cluster analysis to identify cell-cell interactions using cell segments and masks (myeloid and stromal cells).

(B) Left: heatmap showing the relative content of cell types identified in each proximity community cluster. Right: heatmap showing the proportion of myeloid and stromal masks in proximity radius of specified cell community. Each community (one single row) contains both segmented cells from the left heatmap and masks for cell types from the right heatmap. (C, D) IBEX images depicting follicles in non-FL (C) and FL (LN).

(C) non-FL LN with corresponding community plots pseudo-colored as indicated, scale bar 100 μm.

(D) FL LN with corresponding community plots pseudo-colored as indicated, scale bar 100 μm.

(E) Bar plots showing most abundant proximity communities identified by IBEX for the whole imaged section.

(F) Proportion of proximity communities identified by IBEX in the B cell follicles, reflective of whole tissue section.

(G) Distribution of B cell follicle communities across all normal and FL samples based on principal component analysis (PCA). Each symbol represents a follicle from indicated sample, rLN1 (n = 13 follicles).

(H) Community plots from indicated patients. Insets show enlarged images of B cell follicle communities. See also Figure S5 and Table S2.

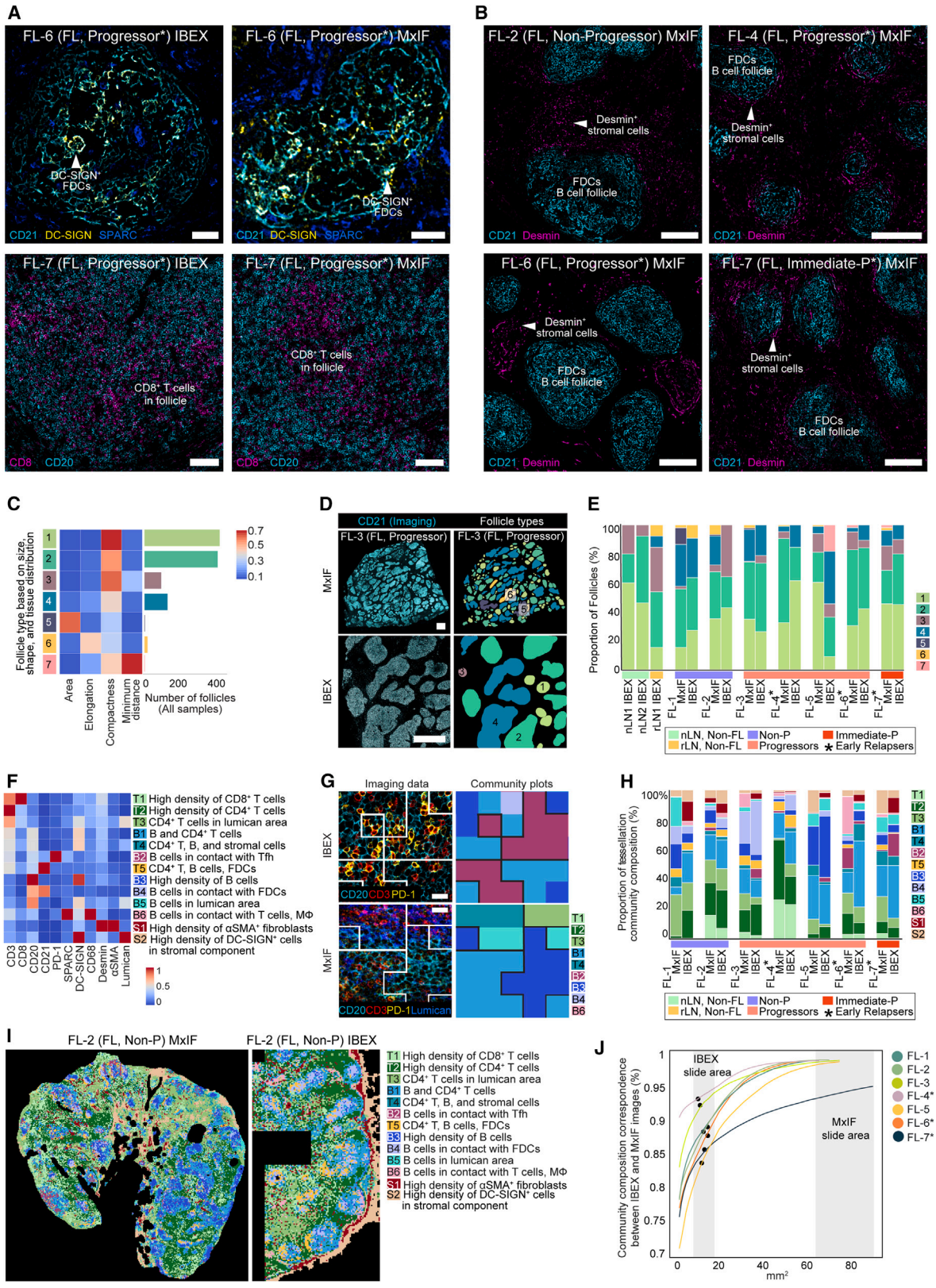

(legend on next page)

of FL B cells.[56] Given previous studies demonstrating spontaneous apoptosis of isolated FL cells *in vitro*, along with the identification of self-reactive tumor cells in FL patients,[42,57] a compelling argument can be made for TME-derived autoantigens driving positive selection of malignant clones. In agreement with other scRNA-seq studies, we observed increased proportions of Tfh cells and T cells expressing markers associated with immune dysfunction and/or exhaustion in FL LNs.[58–61] We also found $CD8^+$ T cells expressing molecules related to cytotoxic T cell function such as *PRF1*, *GZMA*, and *NKG7*.[62,63] The co-expression of markers associated with cytolytic activity and immune inhibition suggests the presence of an anti-FL response that might be re-invigorated for therapeutic purposes. Although initial efforts using T cell-directed cell therapies have shown great promise, mechanisms of immune evasion and resistance are incompletely understood[64] but appear dependent on MHC II expression in the FL TME.[60]

In contrast to previous studies profiling <50,000 cells from dissociated tissues,[58,59] we analyzed 1.8 x 10^6 cells at single-cell and spatial resolution. IBEX spatially resolved myeloid, stromal, and rare (<0.05%) cells that were completely absent or significantly undercounted in RNA-seq datasets. We evaluated changes to the stromal and myeloid components of the FL TME including loss of FDC meshworks, reduction in tingible body macrophages, and expansion of $CD49a^+$ lymphoid stromal cells.[7,35,37,65] The ability to phenotype diverse cell populations across spatial scales—whole tissue sections, major anatomical structures, and proximity communities—presents an opportunity to resolve the confusing literature concerning cellular distribution patterns and clinical outcome in FL.[37,65,66] To this end, we validated unique spatial patterns, such as $DC\text{-}SIGN^+$ FDCs and expansion of FRCs, using orthogonal methods and alternative antibody clones. As an additional resource, we devised analytical approaches to compare morphological features shared between IBEX and MxIF images prepared from the same patient. Here, the shape, size, and distance between B cell follicles yielded a unique structural fingerprint for assessing the similarities between small and large ROIs and additionally offered insights into follicular growth patterns associated with relapse.

A challenge for tumor atlas efforts is to go beyond a detailed description of tissues to a greater understanding of how genetic alterations and spatial patterns contribute to pathogenesis, clonal evolution, and treatment response. Using scRNA-seq, B cells from early relapsers were distinguished for their significant upregulation of pathways involved in BCR signaling, cytokine signaling, and immune activation. Several orthogonal imaging approaches demonstrated FL B cells in contact with $DC\text{-}SIGN^+$ and $vimentin^+$ cells in the TMEs of these patients, providing a potential means of continual BCR engagement through endogenous lectins and/or autoantigens, respectively.[7,39,42,43] FL B cells are known to engage in a bidirectional crosstalk with lymphoid stromal cells, including cytokine/chemokine-producing fibroblasts.[35,54] We hypothesize that these interactions, coupled with matrisome-associated factors produced by FL B cells, results in the expansion and fibrogenic potential of $desmin^+vimentin^+$ fibroblasts in the TMEs of early relapsers. Bulk RNA-seq and IBEX community analysis confirmed the expression of fibroblast and cytokine genes, e.g., TGF-β, known to impact ECM deposition and functional remodeling of LN tissues. As with other cancers,[34] stromal desmoplasia was shown to be a distinctive feature in this study distinguishing early relapsers from other FL patients based on the evaluation of FFPE tissue sections from a larger cohort. Early relapsers were subdivided into two groups, high in S1 or S4 stromal communities, suggesting the possibility of distinct mechanisms of relapse to investigate in future studies. Together, these findings strongly encourage careful examination of anti-fibrotic agents, coupled with therapies that blunt BCR signaling or inhibit DC-SIGN-mediated engagement, for the treatment of FL patients.

In summary, we present a comprehensive molecular and spatial atlas of normal and malignant LNs taken from untreated FL patients in the context of a prospective clinical trial. The extension of our quantitative imaging studies to a greater number of samples with divergent clinical outcomes highlighted the value of this approach by identifying histological patterns of early disease progression and treatment resistance. Most importantly, this work provides a unique opportunity to profile the TMEs of FL patients prior to therapeutic intervention. Despite the urgent clinical need, there are several impediments to the careful examination of relapsed FL including its broad clinical and genetic heterogeneity and challenges with recruiting sufficient numbers of patients with adequate tissue biopsies for large studies.[67] Therefore, this work may inform the selection of novel therapeutic approaches for early relapsers, the highest priority in FL clinical trials.[68]

Limitations of the study

The primary limitation of this study is the evaluation of single biopsies collected from different sites of the human body.

Figure 6. Comparison of spatial patterns and cellular communities between IBEX and MxIF images

(A) Comparison of IBEX and MxIF images for indicated patients. Scale bar (Left, CD21 panels 50 μm; Right, CD8 panels 100 μm).

(B) Confocal images from MxIF samples. Scale bar 200 μm.

(C) Heatmap showing follicle types for all samples.

(D) Follicle composition in representative IBEX and MxIF images, CD21 (cyan), scale bar 1 mm. Bottom row: Follicles color-coded based on types described in C.

(E) Follicle composition of IBEX and MxIF imaged samples. Each bar is a representative tissue section analyzed from an individual sample.

(F) Heatmap of mean mask percentages per tessellation square of markers used to detect tessellation community clusters.

(G) IBEX and MxIF images with corresponding tessellation masks showing community clusters (25 μm). White lines (right) indicate borders of community clusters shown in adjacent plots (left).

(H) Tessellation community plots showing correspondence between IBEX and MxIF images. Each bar is a representative tissue section analyzed from an individual sample.

(I) Tessellation community maps from one representative FL sample.

(J) Percent similarity of IBEX and MxIF community composition depending on the area of tissue imaged and analyzed. Dots indicate the size of the IBEX region of interest. See also Figure S6, Tables S2, and S6.

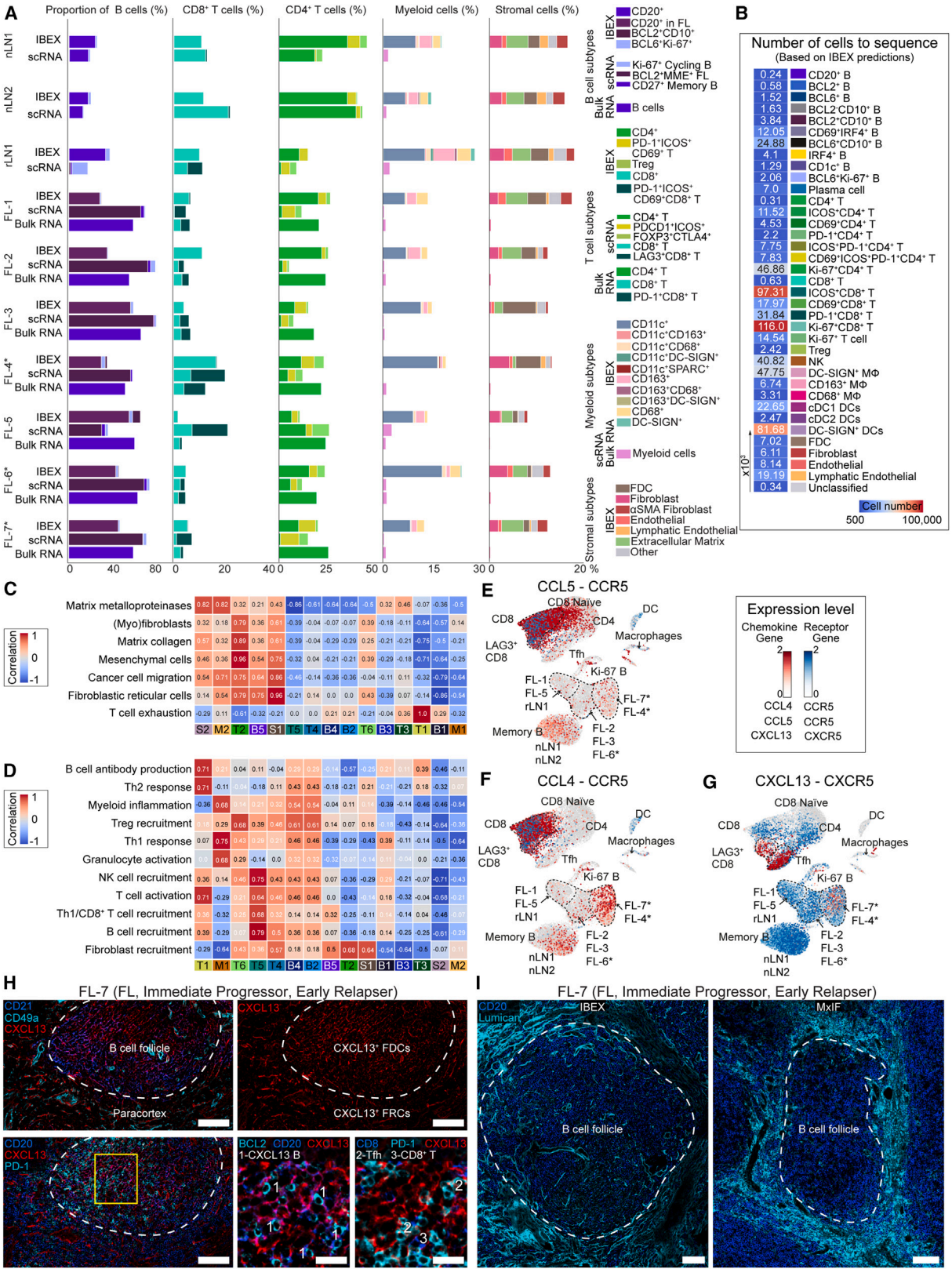

(legend on next page)

While challenging to implement, the intra-tumor heterogeneity observed among FL patients provides significant rationale for multi-site profiling.[59,69] An additional constraint is the lack of paired bulk RNA-seq and MxIF datasets from non-FL LNs due to technical challenges with performing paired analyses from these small LNs. As we did not employ dissociation or enrichment protocols for single-cell analysis of myeloid and stromal cells, these populations are significantly underrepresented in our single-cell datasets as compared to other studies that explicitly examined these populations.[35,54,70] Antibody panel design is a time- and resource-intensive process.[49,50] Due to the lack of suitable reagents, we were limited in the targets examined in our larger cohort. The absence of age, sex, and race and ethnicity-matched clinical groups limits the study's generalization.

STAR★METHODS

Detailed methods are provided in the online version of this paper and include the following:

- KEY RESOURCES TABLE
- RESOURCE AVAILABILITY
  - Lead contact
  - Materials availability
  - Data and code availability
- EXPERIMENTAL MODEL AND STUDY PARTICIPANT DETAILS
- METHOD DETAILS
  - Sample preparation from human tissues
  - Whole exome sequencing (WES) analysis
  - Bulk RNA-seq processing and analyses
  - Deconvolution of bulk RNA-seq
  - scRNA-seq processing and analysis
  - High content imaging using IBEX
  - MxIF imaging of FFPE tissues
  - IBEX and MxIF image acquisition and alignment
  - Object-based segmentation of IBEX images
  - Cell typing of IBEX images
  - Tessellation masks for imaging data
  - Assessment of image analysis workflows
  - Follicles shape analysis
  - Community analysis of IBEX images
  - Slide concordance analysis
  - Number of cells to be sequenced
  - Correlations between single cell communities
  - Cell DIVE-IBEX imaging of FFPE tissues
  - Linear model identifying early relapsers
- QUANTIFICATION AND STATISTICAL ANALYSIS
- ADDITIONAL RESOURCES

SUPPLEMENTAL INFORMATION

Supplemental information can be found online at https://doi.org/10.1016/j.ccell.2024.02.001.

ACKNOWLEDGMENTS

This research was supported by the Intramural Research Program of the NIH, NIAID, and NCI. Z.Y. and B.C.L. are supported by the BCBB Support Services Contract HHSN316201300006W/75N93022F00001 to Guidehouse Inc. D.J. is supported by the grant of the European Research Council (ERC); European Consolidator Grant, XHale (Reference #771883). M.K. is supported by Frederick National Laboratory for Cancer Research contract 75N91019D00024. We are deeply appreciative of Arlene Radtke, Anita Gola, Derek Einhaus, Melinda Angus-Hill, Rick Heil-Chapdelaine, Michael Smith, Prachi Bogetto, Joshua Croteau, Anne Wiblin, and Alexandra Naba for their advice and support.

AUTHOR CONTRIBUTIONS

Conceptualization, A.J.R., E.P., A.B., W.H.W., L.M.S., M.R., and R.N.G.; methodology, A.J.R., E.P., A.V., A.B., M.S., O.K., M.M., M.P., I.G., V.S., S.I., D.W., A. Sharun, A. Sarachakov, G.P., Y.L., E.N., and N.K.; software, E.P., A.V., A.B., M.S., O.K., M.M., M.P., I.G., V.S., S.I., D.W., A. Sharun, A. Sarachakov, G.P., Y.L., Z.Y., B.C.L., E.N., and N.K.; formal analysis, A.J.R., E.P., A.V., A.B., M.S., O.K., M.M., M.P., I.G., V.S., S.I., D.W., A. Sharun, A. Sarachakov, G.P., Y.L., E.N., and N.K.; investigation, A.J.R., E.P., A.V., A.B., M.S., O.K., M.M., M.P., I.G., V.S., S.I., D.W., A. Sharun, A. Sarachakov, G.P., Y.L., Z.Y., B.C.L., E.S., A.L.S., D.W.H., P.O., E.N., N.K., and M.K.; resources, S.P., T.D.-H., K.N., R.A., N.F., J.L.D., J.M.H., W.H.W., E.S.J., L.M.S., M.R., and R.N.G.; writing – original draft, A.J.R.; writing – review and editing, A.J.R., E.P., A.B., Z.Y., E.S., S.P., A.L.S., D.J., J.D.P., K.N., R.A., N.F., J.M.H., W.H.W., E.S.J., L.M.S., M.R., and R.N.G.; visualization, A.J.R., E.P., A.V., A.B., E.S., L.Y., M.S., O.K., M.M., M.P., I.G., V.S., S.I., D.W., A. Sharun, A. Sarachakov, G.P., Y.L., A.L.S., P.O., K.N., E.N., N.K., and R.A.; supervision, A.J.R., E.P., A.B., L.M.S., M.R., and R.N.G.; project administration, A.J.R., E.P., A.B., K.N., and M.R.; funding acquisition, A.B., R.A., N.F., K.N., L.M.S., M.R., and R.N.G.

DECLARATION OF INTERESTS

N.F. is the Chief Medical Officer of BostonGene, Corp., and all authors affiliated with BostonGene, Corp. were employees thereof at the time the study was performed. E.P., A.V., A.B., I.G., V.S., A. Sarachakov, P.O., N.K., and R.A. are inventors of patents related to this work. A.L.S. is an employee and shareholder of AstraZeneca. The follicular lymphoma samples collection conducted at NIAID, NIH, was an investigator-initiated project funded by NIAID, NIH.

Received: July 19, 2022
Revised: December 4, 2023

Figure 7. Data integration reveals extent of stromal undersampling and remodeling in FL TME

(A) Percentage of major cell populations measured by bulk RNA-seq (Bulk RNA), scRNA-seq (scRNA), and IBEX.
(B) Heatmap showing the estimated number of cells to be profiled by scRNA-seq to identify a cluster (cell phenotype) originally identified by IBEX.
(C) Heatmap showing correlations between expression of fibroblast gene signatures measured by bulk RNA-seq with proximity community clusters described in Figure 5.
(D) Heatmap showing correlations between cytokine gene signatures measured by bulk RNA-seq and proximity community clusters described in Figure 5.
(E) UMAP of 36,212 single cells from all samples pseudo-colored for CCR5 (blue) and CCL5 (red) gene expression in the indicated cell types.
(F) UMAP of 36,212 single cells from all samples pseudo-colored for CCR5 (blue) and CCL4 (red) gene expression.
(G) UMAP of 36,212 single cells from all samples pseudo-colored for CXCR5 (blue) and CXCL13 (red) gene expression.
(H) IBEX images demonstrating CXCL13^{+} FDCs and FRCs. Scale bar is 100 μm (large) and 20 μm (small).
(I) IBEX and MxIF images of ECM expansion in one patient sample. Scale bar is 100 μm. See also Figure S7, Tables S2, S7, and S8.

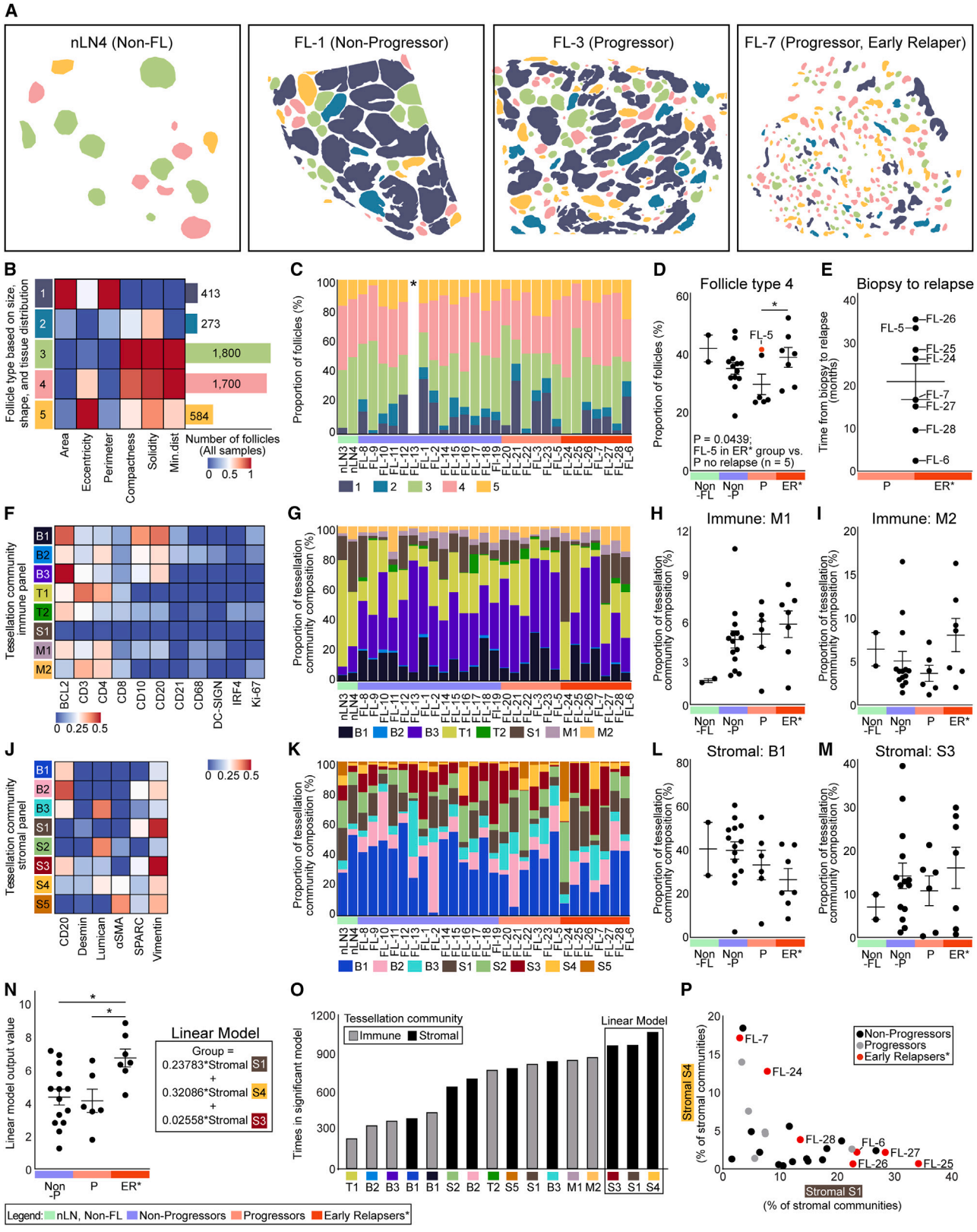

(legend on next page)

Accepted: February 5, 2024
Published: February 29, 2024

REFERENCES

1. HuBMAP Consortium, Lin, S., Posgai, A., Atkinson, M., Regev, A., Rood, J., Rozenblatt-Rosen, O., Gaffney, L., Hupalowska, A., Satija, R., et al. (2019). The human body at cellular resolution: the NIH Human Biomolecular Atlas Program. Nature *574*, 187–192.
2. Jain, S., Pei, L., Spraggins, J.M., Angelo, M., Carson, J.P., Gehlenborg, N., Ginty, F., Gonçalves, J.P., Hagood, J.S., Hickey, J.W., et al. (2023). Advances and prospects for the Human BioMolecular Atlas Program (HuBMAP). Nat. Cell Biol. *25*, 1089–1100.
3. Regev, A., Teichmann, S.A., Lander, E.S., Amit, I., Benoist, C., Birney, E., Bodenmiller, B., Campbell, P., Carninci, P., Clatworthy, M., et al. (2017). The Human Cell Atlas. Elife *6*, e27041.
4. Rozenblatt-Rosen, O., Regev, A., Oberdoerffer, P., Nawy, T., Hupalowska, A., Rood, J.E., Ashenberg, O., Cerami, E., Coffey, R.J., Demir, E., et al. (2020). The Human Tumor Atlas Network: Charting Tumor Transitions across Space and Time at Single-Cell Resolution. Cell *181*, 236–249.
5. Börner, K., Teichmann, S.A., Quardokus, E.M., Gee, J.C., Browne, K., Osumi-Sutherland, D., Herr, B.W., Bueckle, A., Paul, H., Haniffa, M., et al. (2021). Anatomical structures, cell types and biomarkers of the Human Reference Atlas. Nat. Cell Biol. *23*, 1117–1128.
6. Grant, S.M., Lou, M., Yao, L., Germain, R.N., and Radtke, A.J. (2020). The lymph node at a glance – how spatial organization optimizes the immune response. J. Cell Sci. *133*, jcs241828.
7. Carbone, A., Roulland, S., Gloghini, A., Younes, A., von Keudell, G., López-Guillermo, A., and Fitzgibbon, J. (2019). Follicular lymphoma. Nat. Rev. Dis. Prim. *5*, 83.
8. Huet, S., Tesson, B., Jais, J.-P., Feldman, A.L., Magnano, L., Thomas, E., Traverse-Glehen, A., Albaud, B., Carrère, M., Xerri, L., et al. (2018). A gene-expression profiling score for prediction of outcome in patients with follicular lymphoma: a retrospective training and validation analysis in three international cohorts. Lancet Oncol. *19*, 549–561.
9. Scott, D.W., and Gascoyne, R.D. (2014). The tumour microenvironment in B cell lymphomas. Nat. Rev. Cancer *14*, 517–534.
10. Casulo, C., Byrtek, M., Dawson, K.L., Zhou, X., Farber, C.M., Flowers, C.R., Hainsworth, J.D., Maurer, M.J., Cerhan, J.R., Link, B.K., et al. (2015). Early Relapse of Follicular Lymphoma After Rituximab Plus Cyclophosphamide, Doxorubicin, Vincristine, and Prednisone Defines Patients at High Risk for Death: An Analysis From the National LymphoCare Study. J. Clin. Oncol. *33*, 2516–2522.
11. Potts, D.A., Fromm, J.R., Gopal, A.K., and Cassaday, R.D. (2017). Spontaneous Remission of an Untreated, MYC and BCL2 Coexpressing, High-Grade B-Cell Lymphoma: A Case Report and Literature Review. Case Rep. Hematol. *2017*, 2676254.
12. Casulo, C., Dixon, J.G., Le-Rademacher, J., Hoster, E., Hochster, H.S., Hiddemann, W., Marcus, R., Kimby, E., Herold, M., Sebban, C., et al. (2022). Validation of POD24 As a Robust Early Clinical Endpoint of Poor Survival in FL from 5,225 Patients on 13 Clinical Trials. Blood *139*, 1684–1693.
13. Rodgers, T.D., Casulo, C., Boissard, F., Launonen, A., Parreira, J., and Cartron, G. (2021). Early Relapse in First-Line Follicular Lymphoma: A Review of the Clinical Implications and Available Mitigation and Management Strategies. Oncol. Ther. *9*, 329–346.
14. Freeman, C.L., Kridel, R., Moccia, A.A., Savage, K.J., Villa, D.R., Scott, D.W., Gerrie, A.S., Ferguson, D., Cafferty, F., Slack, G.W., et al. (2019). Early progression after bendamustine-rituximab is associated with high risk of transformation in advanced stage follicular lymphoma. Blood *134*, 761–764.
15. Maurer, M.J., Bachy, E., Ghesquières, H., Ansell, S.M., Nowakowski, G.S., Thompson, C.A., Inwards, D.J., Allmer, C., Chassagne-Clément, C., Nicolas-Virelizier, E., et al. (2016). Early event status informs subsequent outcome in newly diagnosed follicular lymphoma. Am. J. Hematol. *91*, 1096–1101.
16. Lackraj, T., Goswami, R., and Kridel, R. (2018). Pathogenesis of follicular lymphoma. Best Pract. Res. Clin. Haematol. *31*, 2–14.
17. Kridel, R., Chan, F.C., Mottok, A., Boyle, M., Farinha, P., Tan, K., Meissner, B., Bashashati, A., McPherson, A., Roth, A., et al. (2016). Histological Transformation and Progression in Follicular Lymphoma: A Clonal Evolution Study. PLoS Med. *13*, e1002197.
18. Dave, S.S., Wright, G., Tan, B., Rosenwald, A., Gascoyne, R.D., Chan, W.C., Fisher, R.I., Braziel, R.M., Rimsza, L.M., Grogan, T.M., et al. (2004). Prediction of survival in follicular lymphoma based on molecular features of tumor-infiltrating immune cells. N. Engl. J. Med. *351*, 2159–2169.
19. Radtke, A., and Roschewski, M. (2024). The follicular lymphoma tumor microenvironment at single cell and spatial resolution. Blood *1*, blood.2023020999.
20. Radtke, A.J., Kandov, E., Lowekamp, B., Speranza, E., Chu, C.J., Gola, A., Thakur, N., Shih, R., Yao, L., Yaniv, Z.R., et al. (2020). IBEX: A versatile multiplex optical imaging approach for deep phenotyping and spatial analysis of cells in complex tissues. Proc. Natl. Acad. Sci. USA *117*, 33455–33465.
21. Radtke, A.J., Chu, C.J., Yaniv, Z., Yao, L., Marr, J., Beuschel, R.T., Ichise, H., Gola, A., Kabat, J., Lowekamp, B., et al. (2022). IBEX: an iterative

Figure 8. Changes in follicle composition and increased stromal remodeling in high-risk FL patients

(A) Follicle composition based on Cell DIVE-IBEX images and classifications in B.
(B) Heatmap of follicle types based on indicated parameters.
(C) Follicle composition for all samples. No follicles: FL-13 (*).
(D) Proportion of follicle type 4 for all samples with FL-5 analyzed with early relapsers.
(E) Time (months) from biopsy to relapse for indicated patients.
(F) Heatmap of mean mask percentages per tessellation square for immune panel.
(G) Tessellation community plots for communities in F. Graphs depicting the proportion of M1.
(H) Proportion of M1 tesselation community per sample.
(I) Proportion of M2 tesselation community per sample.
(J) Heatmap of mean mask percentages per tessellation square for stromal panel.
(K) Tessellation community plots for communities in J. Graphs depicting the proportion of B1.
(L) Proportion of B1 tesselation community per sample.
(M) Proportion of S3 tesselation community per sample. See also Figures S1, S8, Tables S1, and S2.
(N) Description and statistical analysis of significant generalized linear model distinguishing early relapsers from other FL patients, p value = 0.0235.
(O) Communities ranked by the number of times they appear in a significant model (determined by the intercept p value being <0.1).
(P) Distribution of samples based on the proportion of S4 and S1 communities in K. For all dotplots, data represented as mean ± SEM. Each symbol is a representative tissue section analyzed from an individual sample (n = 29).
(D and N) ANOVA (Kruskal-Wallis test) with Benjamini-Hochberg method for false discovery rate (FDR) to correct p values for multiple comparisons. See also Figure S8 and Tables S1 and S6.

immunolabeling and chemical bleaching method for high-content imaging of diverse tissues. Nat. Protoc. *17*, 378–401.

22. Gerdes, M.J., Sevinsky, C.J., Sood, A., Adak, S., Bello, M.O., Bordwell, A., Can, A., Corwin, A., Dinn, S., Filkins, R.J., et al. (2013). Highly multiplexed single-cell analysis of formalin-fixed, paraffin-embedded cancer tissue. Proc. Natl. Acad. Sci. USA *110*, 11982–11987.
23. Zaytcev, A., Chelushkin, M., Nuzhdina, K., Bagaev, A., Dyykanov, D., Zyrin, V., Paul, S.R., Davies, D.L., Reeves, P.M., Lanuti, M., et al. (2020). Abstract 853: Novel machine learning based deconvolution algorithm results in accurate description of tumor microenvironment from bulk RNAseq. Cancer Res. *80*, 853.
24. Bolotin, D.A., Poslavsky, S., Davydov, A.N., Frenkel, F.E., Fanchi, L., Zolotareva, O.I., Hemmers, S., Putintseva, E.V., Obraztsova, A.S., Shugay, M., et al. (2017). Antigen receptor repertoire profiling from RNA-seq data. Nat. Biotechnol. *35*, 908–911.
25. Waise, S., Parker, R., Rose-Zerilli, M.J.J., Layfield, D.M., Wood, O., West, J., Ottensmeier, C.H., Thomas, G.J., and Hanley, C.J. (2019). An optimised tissue disaggregation and data processing pipeline for characterising fibroblast phenotypes using single-cell RNA sequencing. Sci. Rep. *9*, 9580.
26. Korotkevich, G., Sukhov, V., Budin, N., Shpak, B., Artyomov, M.N., and Sergushichev, A. (2021). Fast gene set enrichment analysis. Preprint at bioRxiv. https://doi.org/10.1101/060012.
27. Wang, Z., Liu, F., Fan, N., Zhou, C., Li, D., Macvicar, T., Dong, Q., Bruns, C.J., and Zhao, Y. (2020). Targeting Glutaminolysis: New Perspectives to Understand Cancer Development and Novel Strategies for Potential Target Therapies. Front. Oncol. *10*, 589508.
28. Naba, A., Clauser, K.R., Hoersch, S., Liu, H., Carr, S.A., and Hynes, R.O. (2012). The matrisome: in silico definition and in vivo characterization by proteomics of normal and tumor extracellular matrices. Mol. Cell. Proteomics *11*, M111.014647.
29. Wang, L., Yao, Z.Q., Moorman, J.P., Xu, Y., and Ning, S. (2014). Gene expression profiling identifies IRF4-associated molecular signatures in hematological malignancies. PLoS One *9*, e106788.
30. Mottok, A., Jurinovic, V., Farinha, P., Rosenwald, A., Leich, E., Ott, G., Horn, H., Klapper, W., Boesl, M., Hiddemann, W., et al. (2018). FOXP1 expression is a prognostic biomarker in follicular lymphoma treated with rituximab and chemotherapy. Blood *131*, 226–235.
31. Küppers, R., and Stevenson, F.K. (2018). Critical influences on the pathogenesis of follicular lymphoma. Blood *131*, 2297–2306.
32. Jorgensen, M., Radtke, A.J., and Wasserfall, C. (2021). HuBMAP ASCT+B Tables. Lymph Node v1.0.
33. Germain, R.N., Radtke, A.J., Thakur, N., Schrom, E.C., Hor, J.L., Ichise, H., Arroyo-Mejias, A.J., Chu, C.J., and Grant, S. (2022). Understanding immunity in a tissue-centric context: Combining novel imaging methods and mathematics to extract new insights into function and dysfunction. Immunol. Rev. *306*, 8–24.
34. Risom, T., Glass, D.R., Averbukh, I., Liu, C.C., Baranski, A., Kagel, A., McCaffrey, E.F., Greenwald, N.F., Rivero-Gutiérrez, B., Strand, S.H., et al. (2022). Transition to invasive breast cancer is associated with progressive changes in the structure and composition of tumor stroma. Cell *185*, 299–310.e18.
35. Mourcin, F., Verdière, L., Roulois, D., Amin, R., Lamaison, C., Sibut, V., Thamphya, B., Pangault, C., Monvoisin, C., Huet, S., et al. (2021). Follicular lymphoma triggers phenotypic and functional remodeling of the human lymphoid stromal cell landscape. Immunity *54*, 1788–1806.e7.
36. Farinha, P., Al-Tourah, A., Gill, K., Klasa, R., Connors, J.M., and Gascoyne, R.D. (2010). The architectural pattern of FOXP3-positive T cells in follicular lymphoma is an independent predictor of survival and histologic transformation. Blood *115*, 289–295.
37. Kridel, R., Sehn, L.H., and Gascoyne, R.D. (2017). Can histologic transformation of follicular lymphoma be predicted and prevented? Blood *130*, 258–266.
38. Sayin, I., Radtke, A.J., Vella, L.A., Jin, W., Wherry, E.J., Buggert, M., Betts, M.R., Herati, R.S., Germain, R.N., and Canaday, D.H. (2018). Spatial distribution and function of T follicular regulatory cells in human lymph nodes. J. Exp. Med. *215*, 1531–1542.
39. Amin, R., Mourcin, F., Uhel, F., Pangault, C., Ruminy, P., Dupré, L., Guirriec, M., Marchand, T., Fest, T., Lamy, T., and Tarte, K. (2015). DC-SIGN–expressing macrophages trigger activation of mannosylated IgM B-cell receptor in follicular lymphoma. Blood *126*, 1911–1920.
40. Coelho, V., Krysov, S., Ghaemmaghami, A.M., Emara, M., Potter, K.N., Johnson, P., Packham, G., Martinez-Pomares, L., and Stevenson, F.K. (2010). Glycosylation of surface Ig creates a functional bridge between human follicular lymphoma and microenvironmental lectins. Proc. Natl. Acad. Sci. USA *107*, 18587–18592.
41. Hsi, E.D., Rimsza, L., Goldman, B.H., Cook, J.R., Tubbs, R.R., Press, O.W., Maloney, D.G., Fisher, R.I., and Sweetenham, J. (2008). MUM1 Expression in Follicular Lymphoma Is a Poor Prognostic Marker in Patients Treated with Immunochemotherapy (SWOG 9800/9911) but Not Chemotherapy Alone (SWOG 8809): A Southwest Oncology Group Correlative Science Study. Blood *112*, 376.
42. Cha, S.-C., Qin, H., Kannan, S., Rawal, S., Watkins, L.S., Baio, F.E., Wu, W., Ong, J., Wei, J., Kwak, B., et al. (2013). Nonstereotyped Lymphoma B Cell Receptors Recognize Vimentin as a Shared Autoantigen. J. Immunol. *190*, 4887–4898.
43. Shukla, V., and Lu, R. (2014). IRF4 and IRF8: Governing the virtues of B Lymphocytes. Front. Biol. *9*, 269–282.
44. Goltsev, Y., Samusik, N., Kennedy-Darling, J., Bhate, S., Hale, M., Vazquez, G., Black, S., and Nolan, G.P. (2018). Deep Profiling of Mouse Splenic Architecture with CODEX Multiplexed Imaging. Cell *174*, 968–981.e15.
45. Nagarsheth, N., Wicha, M.S., and Zou, W. (2017). Chemokines in the cancer microenvironment and their relevance in cancer immunotherapy. Nat. Rev. Immunol. *17*, 559–572.
46. Prud'homme, G.J. (2007). Pathobiology of transforming growth factor β in cancer, fibrosis and immunologic disease, and therapeutic considerations. Lab. Invest. *87*, 1077–1091.
47. Luzina, I.G., Todd, N.W., Sundararajan, S., and Atamas, S.P. (2015). The cytokines of pulmonary fibrosis: Much learned, much more to learn. Cytokine *74*, 88–100.
48. Husson, H., Freedman, A.S., Cardoso, A.A., Strola, G., Munoz, O., Carideo, E.G., De Beaumont, R., Caligaris-Cappio, F., et al. (2002). CXCL13 (BCA-1) is produced by follicular lymphoma cells: role in the accumulation of malignant B cells. Br. J. Haematol. *119*, 492–495.
49. Hickey, J.W., Neumann, E.K., Radtke, A.J., Camarillo, J.M., Beuschel, R.T., Albanese, A., McDonough, E., Hatler, J., Wiblin, A.E., Fisher, J., et al. (2022). Spatial mapping of protein composition and tissue organization: a primer for multiplexed antibody-based imaging. Nat. Methods *19*, 284–295.
50. Quardokus, E.M., Saunders, D.C., McDonough, E., Hickey, J.W., Werlein, C., Surrette, C., Rajbhandari, P., Casals, A.M., Tian, H., Lowery, L., et al. (2023). Organ Mapping Antibody Panels: a community resource for standardized multiplexed tissue imaging. Nat. Methods *20*, 1174–1178.
51. Wong, S.L.I., and Sukkar, M.B. (2017). The SPARC protein: an overview of its role in lung cancer and pulmonary fibrosis and its potential role in chronic airways disease. Br. J. Pharmacol. *174*, 3–14.
52. Rood, J.E., Maartens, A., Hupalowska, A., Teichmann, S.A., and Regev, A. (2022). Impact of the Human Cell Atlas on medicine. Nat. Med. *28*, 2486–2496.
53. Madsen, C., Lauridsen, K.L., Plesner, T.L., Monrad, I., Honoré, B., Hamilton-Dutoit, S., d'Amore, F., and Ludvigsen, M. (2019). High intratumoral expression of vimentin predicts histological transformation in patients with follicular lymphoma. Blood Cancer J. *9*, 35.
54. Abe, Y., Sakata-Yanagimoto, M., Fujisawa, M., Miyoshi, H., Suehara, Y., Hattori, K., Kusakabe, M., Sakamoto, T., Nishikii, H., Nguyen, T.B., et al.

(2022). A single-cell atlas of non-haematopoietic cells in human lymph nodes and lymphoma reveals a landscape of stromal remodelling. Nat. Cell Biol. *24*, 565–578.

55. Hwang, B., Lee, J.H., and Bang, D. (2018). Single-cell RNA sequencing technologies and bioinformatics pipelines. Exp. Mol. Med. *50*, 1–14.
56. Bahler, D.W., Zelenetz, A.D., Chen, T.T., and Levy, R. (1992). Antigen selection in human lymphomagenesis. Cancer Res. *52*, 5547s–5551s.
57. Sachen, K.L., Strohman, M.J., Singletary, J., Alizadeh, A.A., Kattah, N.H., Lossos, C., Mellins, E.D., Levy, S., and Levy, R. (2012). Self-antigen recognition by follicular lymphoma B-cell receptors. Blood *120*, 4182–4190.
58. Andor, N., Simonds, E.F., Czerwinski, D.K., Chen, J., Grimes, S.M., Wood-Bouwens, C., Zheng, G.X.Y., Kubit, M.A., Greer, S., Weiss, W.A., et al. (2019). Single-cell RNA-Seq of follicular lymphoma reveals malignant B-cell types and coexpression of T-cell immune checkpoints. Blood *133*, 1119–1129.
59. Haebe, S., Shree, T., Sathe, A., Day, G., Czerwinski, D.K., Grimes, S.M., Lee, H., Binkley, M.S., Long, S.R., Martin, B., et al. (2021). Single-cell analysis can define distinct evolution of tumor sites in follicular lymphoma. Blood *137*, 2869–2880.
60. Han, G., Deng, Q., Marques-Piubelli, M.L., Dai, E., Dang, M., Ma, M.C.J., Li, X., Yang, H., Henderson, J., Kudryashova, O., et al. (2022). Follicular Lymphoma Microenvironment Characteristics Associated with Tumor Cell Mutations and MHC Class II Expression. Blood Cancer Discov. *3*, 428–443.
61. Armengol, M., Santos, J.C., Fernández-Serrano, M., Profitós-Pelejà, N., Ribeiro, M.L., and Roué, G. (2021). Immune-Checkpoint Inhibitors in B-Cell Lymphoma. Cancers *13*, 214.
62. Ng, S.S., De Labastida Rivera, F., Yan, J., Corvino, D., Das, I., Zhang, P., Kuns, R., Chauhan, S.B., Hou, J., Li, X.-Y., et al. (2020). The NK cell granule protein NKG7 regulates cytotoxic granule exocytosis and inflammation. Nat. Immunol. *21*, 1205–1218.
63. Szabo, P.A., Levitin, H.M., Miron, M., Snyder, M.E., Senda, T., Yuan, J., Cheng, Y.L., Bush, E.C., Dogra, P., Thapa, P., et al. (2019). Single-cell transcriptomics of human T cells reveals tissue and activation signatures in health and disease. Nat. Commun. *10*, 4706.
64. Fowler, N.H., Dickinson, M., Dreyling, M., Martinez-Lopez, J., Kolstad, A., Butler, J., Ghosh, M., Popplewell, L., Chavez, J.C., Bachy, E., et al. (2022). Tisagenlecleucel in adult relapsed or refractory follicular lymphoma: the phase 2 ELARA trial. Nat. Med. *28*, 325–332.
65. Verdière, L., Mourcin, F., and Tarte, K. (2018). Microenvironment signaling driving lymphomagenesis. Curr. Opin. Hematol. *25*, 335–345.
66. Glas, A.M., Knoops, L., Delahaye, L., Kersten, M.J., Kibbelaar, R.E., Wessels, L.A., van Laar, R., van Krieken, J.H.J.M., Baars, J.W., Raemaekers, J., et al. (2007). Gene-expression and immunohistochemical study of specific T-cell subsets and accessory cell types in the transformation and prognosis of follicular lymphoma. J. Clin. Oncol. *25*, 390–398.
67. Rodgers, T.D., and Barr, P.M. (2021). Management of relapsed follicular lymphoma. Ann. Lymphoma *5*, 14.
68. Maddocks, K., Barr, P.M., Cheson, B.D., Little, R.F., Baizer, L., Kahl, B.S., Leonard, J.P., Fowler, N., Gordon, L.I., Link, B.K., et al. (2017). Recommendations for Clinical Trial Development in Follicular Lymphoma. J. Natl. Cancer Inst. *109*, djw255.
69. Araf, S., Wang, J., Korfi, K., Pangault, C., Kotsiou, E., Rio-Machin, A., Rahim, T., Heward, J., Clear, A., Iqbal, S., et al. (2018). Genomic profiling reveals spatial intra-tumor heterogeneity in follicular lymphoma. Leukemia *32*, 1261–1265.
70. Buechler, M.B., Pradhan, R.N., Krishnamurty, A.T., Cox, C., Calviello, A.K., Wang, A.W., Yang, Y.A., Tam, L., Caothien, R., Roose-Girma, M., et al. (2021). Cross-tissue organization of the fibroblast lineage. Nature *593*, 575–579.
71. Cheson, B.D., Fisher, R.I., Barrington, S.F., Cavalli, F., Schwartz, L.H., Zucca, E., Lister, T.A., et al.; Alliance Australasian Leukaemia and Lymphoma Group; European Mantle Cell Lymphoma Consortium (2014). Recommendations for initial evaluation, staging, and response assessment of Hodgkin and non-Hodgkin lymphoma: the Lugano classification. J. Clin. Oncol. *32*, 3059–3068.
72. Solal-Céligny, P., Roy, P., Colombat, P., White, J., Armitage, J.O., Arranz-Saez, R., Au, W.Y., Bellei, M., Brice, P., Caballero, D., et al. (2004). Follicular lymphoma international prognostic index. Blood *104*, 1258–1265.
73. Allahyar, A., Pieterse, M., Swennenhuis, J., Los-de Vries, G.T., Yilmaz, M., Leguit, R., Meijers, R.W.J., van der Geize, R., Vermaat, J., Cleven, A., et al. (2021). Robust detection of translocations in lymphoma FFPE samples using targeted locus capture-based sequencing. Nat. Commun. *12*, 3361.
74. Jonigk, D., Modde, F., Bockmeyer, C.L., Becker, J.U., and Lehmann, U. (2011). Optimized RNA extraction from non-deparaffinized, laser-microdissected material. Methods Mol. Biol. *755*, 67–75.
75. Bushnell, B. (2014). BBMap: A Fast, Accurate, Splice-Aware Aligner (Lawrence Berkeley National Laboratory). LBNL Report #: LBNL-7065E.
76. Li, H., and Durbin, R. (2009). Fast and accurate short read alignment with Burrows-Wheeler transform. Bioinformatics *25*, 1754–1760.
77. Auwera, G.v.d., and O'Connor, B.D. (2020). Genomics in the Cloud : Using Docker, GATK, and WDL in Terra, First edition (O'Reilly Media).
78. Saunders, C.T., Wong, W.S.W., Swamy, S., Becq, J., Murray, L.J., and Cheetham, R.K. (2012). Strelka: accurate somatic small-variant calling from sequenced tumor–normal sample pairs. Bioinformatics *28*, 1811–1817.
79. Goldman, M.J., Craft, B., Hastie, M., Repečka, K., McDade, F., Kamath, A., Banerjee, A., Luo, Y., Rogers, D., Brooks, A.N., et al. (2020). Visualizing and interpreting cancer genomics data via the Xena platform. Nat. Biotechnol. *38*, 675–678.
80. Zaitsev, A., Chelushkin, M., Dyikanov, D., Cheremushkin, I., Shpak, B., Nomie, K., Zyrin, V., Nuzhdina, E., Lozinsky, Y., Zotova, A., et al. (2022). Precise reconstruction of the TME using bulk RNA-seq and a machine learning algorithm trained on artificial transcriptomes. Cancer Cell *40*, 879–894.e16.
81. Racle, J., de Jonge, K., Baumgaertner, P., Speiser, D.E., and Gfeller, D. (2017). Simultaneous enumeration of cancer and immune cell types from bulk tumor gene expression data. Elife *6*, e26476.
82. Hänzelmann, S., Castelo, R., and Guinney, J. (2013). GSVA: gene set variation analysis for microarray and RNA-Seq data. BMC Bioinf. *14*, 7.
83. Luecken, M.D., and Theis, F.J. (2019). Current best practices in single-cell RNA-seq analysis: a tutorial. Mol. Syst. Biol. *15*, e8746.
84. Wolf, F.A., Angerer, P., and Theis, F.J. (2018). SCANPY: large-scale single-cell gene expression data analysis. Genome Biol. *19*, 15.
85. Stuart, T., Butler, A., Hoffman, P., Hafemeister, C., Papalexi, E., Mauck, W.M., 3rd, Hao, Y., Stoeckius, M., Smibert, P., and Satija, R. (2019). Comprehensive Integration of Single-Cell Data. Cell *177*, 1888–1902.e21.
86. Traag, V.A., Waltman, L., and van Eck, N.J. (2019). From Louvain to Leiden: guaranteeing well-connected communities. Sci. Rep. *9*, 5233.
87. Bolotin, D.A., Poslavsky, S., Mitrophanov, I., Shugay, M., Mamedov, I.Z., Putintseva, E.V., and Chudakov, D.M. (2015). MiXCR: software for comprehensive adaptive immunity profiling. Nat. Methods *12*, 380–381.
88. Liberzon, A., Birger, C., Thorvaldsdóttir, H., Ghandi, M., Mesirov, J.P., and Tamayo, P. (2015). The Molecular Signatures Database (MSigDB) hallmark gene set collection. Cell Syst. *1*, 417–425.
89. Hao, Y., Hao, S., Andersen-Nissen, E., Mauck, W.M., 3rd, Zheng, S., Butler, A., Lee, M.J., Wilk, A.J., Darby, C., Zager, M., et al. (2021). Integrated analysis of multimodal single-cell data. Cell *184*, 3573–3587.e29.
90. Wickham, H. (2016). ggplot2:Elegant Graphics for Data Analysis. Use R!, 2nd edition (Springer International Publishing: Imprint:Springer).
91. Lowekamp, B.C., Chen, D.T., Ibáñez, L., and Blezek, D. (2013). The Design of SimpleITK. Front. Neuroinf. *7*, 45.

92. Yaniv, Z., Lowekamp, B.C., Johnson, H.J., and Beare, R. (2018). SimpleITK Image-Analysis Notebooks: a Collaborative Environment for Education and Reproducible Research. J. Digit. Imag. *31*, 290–303.

93. Guizar-Sicairos, M., Thurman, S.T., and Fienup, J.R. (2008). Efficient subpixel image registration algorithms. Opt. Lett. *33*, 156–158.

94. He, K., Gkioxari, G., Dollár, P., and Girshick, R. (2017). Mask R-CNN, pp. 2980–2988.

95. Otsu, N. (1979). A threshold selection method from gray-level histograms. IEEE Trans. Syst. Man Cybern. *9*, 62–66.

96. Schindelin, J., Arganda-Carreras, I., Frise, E., Kaynig, V., Longair, M., Pietzsch, T., Preibisch, S., Rueden, C., Saalfeld, S., Schmid, B., et al. (2012). Fiji: an open-source platform for biological-image analysis. Nat. Methods *9*, 676–682.

97. Levine, J.H., Simonds, E.F., Bendall, S.C., Davis, K.L., Amir, E.a.D., Tadmor, M.D., Litvin, O., Fienberg, H.G., Jager, A., Zunder, E.R., et al. (2015). Data-Driven Phenotypic Dissection of AML Reveals Progenitor-like Cells that Correlate with Prognosis. Cell *162*, 184–197.

98. Bannon, D., Moen, E., Schwartz, M., Borba, E., Kudo, T., Greenwald, N., Vijayakumar, V., Chang, B., Pao, E., Osterman, E., et al. (2021). DeepCell Kiosk: scaling deep learning–enabled cellular image analysis with Kubernetes. Nat. Methods *18*, 43–45.

99. Schmidt, U., Weigert, M., Broaddus, C., and Myers, G. (2018). In Cell Detection with Star-Convex Polygons. held in Cham, 2018//, A.F. Frangi, J.A. Schnabel, C. Davatzikos, C. Alberola-López, and G. Fichtinger, eds. (Springer International Publishing), pp. 265–273.

100. Zarubin, D., Belotskiy, V., Xiang, Z., Varlamova, A., Ovcharov, P., Galkin, I., Polyakova, M., Svekolkin, V., Perelman, G., Bruttan, M., et al. (2022). A clinical AI-driven multiplex immunofluorescence imaging pipeline to characterize tumor microenvironment heterogeneity. J. Clin. Oncol. *40*, 3020.

101. Ward, J.H., Jr. (1963). Hierarchical grouping to optimize an objective function. J. Am. Stat. Assoc. *58*, 236–244.

102. Virtanen, P., Gommers, R., Oliphant, T.E., Haberland, M., Reddy, T., Cournapeau, D., Burovski, E., Peterson, P., Weckesser, W., Bright, J., et al. (2020). SciPy 1.0: fundamental algorithms for scientific computing in Python. Nat. Methods *17*, 261–272.

103. Pan, S., Hu, R., Long, G., Jiang, J., Yao, L., and Zhang, C. (2018). Adversarially regularized graph autoencoder for graph embedding. Preprint at arXiv. https://doi.org/10.48550/arXiv.1802.04407.

104. Fey, M., and Lenssen, J.E. (2019). Fast Graph Representation Learning with PyTorch Geometric. Preprint at ArXiv. https://doi.org/10.48550/arXiv.1903.02428.

105. Kamp, J.C., Neubert, L., Stark, H., Hinrichs, J.B., Boekhoff, C., Seidel, A.D., Ius, F., Haverich, A., Gottlieb, J., Welte, T., et al. (2022). Comparative Analysis of Gene Expression in Fibroblastic Foci in Patients with Idiopathic Pulmonary Fibrosis and Pulmonary Sarcoidosis. Cells *11*, 664.

106. Jonigk, D., Stark, H., Braubach, P., Neubert, L., Shin, H.O., Izykowski, N., Welte, T., Janciauskiene, S., Warnecke, G., Haverich, A., et al. (2019). Morphological and molecular motifs of fibrosing pulmonary injury patterns. J. Pathol. Clin. Res. *5*, 256–271.

107. Yaniv, Z., Anidi, I., Arrakal, L., Arroyo-Mejias, A., Beuschel, R., Börner, K., Colin, C., Clatworthy, M., Colautti, J., Croteau, J., et al. (2023). Iterative Bleaching Extends Multiplexity (IBEX) Knowledge-Base. https://zenodo.org/records/7693279.

108. Can, A., Bello, M., Cline, H.E., Xiaodong, T., Ginty, F., Sood, A., Gerdes, M., and Montalto, M. (2008). Multi-modal Imaging of Histological Tissue Sections, pp. 288–291.

109. Fletcher, A.L., Acton, S.E., and Knoblich, K. (2015). Lymph node fibroblastic reticular cells in health and disease. Nat. Rev. Immunol. *15*, 350–361.

110. Chhabra, Y., and Weeraratna, A.T. (2023). Fibroblasts in cancer: Unity in heterogeneity. Cell *186*, 1580–1609.

111. Mor-Vaknin, N., Punturieri, A., Sitwala, K., and Markovitz, D.M. (2003). Vimentin is secreted by activated macrophages. Nat. Cell Biol. *5*, 59–63.

STAR★METHODS

KEY RESOURCES TABLE

REAGENT or RESOURCE	SOURCE	IDENTIFIER
Antibodies		
CD20 (clone L26)	Ventana Medical Systems	Cat# 760–2531; RRID: AB_2335956
CD10 (clone SP67)	Ventana Medical Systems	Cat# 790–4506; RRID: AB_2336021
CD3 (clone 2GV6)	Ventana Medical Systems	Cat# 790–4341; RRID: AB_2335978
BCL2 (clone SP66)	Ventana Medical Systems	Cat# 790–4604; RRID: N/A
BCL6 (clone EP278)	Cell Marque	Cat# 227R-28; RRID: N/A
Ki-67 (clone MIB-1)	Agilent	Cat# M7240; RRID: AB_2142367
CD21 (clone EP3093)	Ventana Medical Systems	Cat# 760–4438; RRID: N/A
CD23 (clone IB12)	Leica Biosystems	Cat# NCL-CD23-1B12; RRID: AB_442058
IgD (clone 92)	Agilent	Cat# A0093; RRID: N/A
CD20 AF488 (clone L26)	Thermo Fisher Scientific	Cat# 53-0202-82; RRID: AB_10734358
CD20 eF660 (clone L26)	Thermo Fisher Scientific	Cat# 50-0202-82; RRID: AB_11150959
SPARC AF532 (goat polyclonal, custom conjugate from company)	R&D Systems	Cat# N/A; RRID: AB_ 2892754
CD10 PE (clone FR4D11)	Caprico Biotechnologies	Cat# 103926; RRID: N/A
CD10 PE (clone HI10a)	BioLegend	Cat# 312204; RRID: AB_314915
CD3 AF594 (clone UCHT1)	BioLegend	Cat# 300446; RRID: AB_2563236
BCL2 AF647(clone 100)	BioLegend	Cat# 658705; RRID: AB_2563279
Collagen IV (rabbit polyclonal)	Abcam	Cat# Ab6586; RRID: AB_305584
Goat anti-rabbit IgG AF700	Thermo Fisher Scientific	Cat# A21038; RRID: AB_2535709
IgD AF488 (clone IA6-2)	BioLegend	Cat# 348216; RRID: AB_11150595
CD21 AF532 (clone Bu32), custom conjugate from company	BioLegend	Cat# N/A; RRID: AB_2892739
CD138 PE (clone MI15)	BioLegend	Cat# 356504; RRID: AB_2561878
BCL6 AF647 (clone K112-91)	BD Biosciences	Cat# 561525; RRID: AB_10898007
CD31 AF700 (clone WM59)	BioLegend	Cat# 303133; RRID: AB_2566326
HLA-DR AF488 (clone L243)	BioLegend	Cat# 307620; RRID: AB_493175
CD23 AF532 (clone EBVCS-5), custom conjugate from company	BioLegend	Cat# N/A; RRID: AB_2892740
CD1c PE (clone L161)	BioLegend	Cat# 331506; RRID: AB_1088999
CD163 AF647 (clone GH1/61)	BioLegend	Cat# 333620; RRID: AB_2563475
CD11c AF700 (clone B-Ly6)	BD Biosciences	Cat# 561352; RRID: AB_10612006
CD8 AF488 (clone SK1)	BioLegend	Cat# 344716; RRID: AB_10549301
CD4 AF532 (clone RPA-T4)	Thermo Fisher Scientific	Cat# 58-0049-42; RRID: AB_2802361
FOXP3 eF570 (clone 236A/E7)	Thermo Fisher Scientific	Cat# 41-4777-82; RRID: AB_2573609
CD25 AF647 (clone M-A251)	BioLegend	Cat# 356128; RRID: AB_2563588
Ki-67 AF700 (clone B56)	BD Biosciences	Cat# 561277; RRID: AB_10611571
ICOS AF488 (clone CS98.4A)	BioLegend	Cat# 313514; RRID: AB_2122584
SPARC AF532 (goat polyclonal, custom conjugate from company based on Cat#AF941)	R&D Systems	Cat# N/A; RRID: AB_2892754
PD-1 PE (clone EH12.2H7)	BioLegend	Cat# 329906; RRID: AB_940483
CD69 AF647 (clone FN50)	BioLegend	Cat# 310918; RRID: AB_528871
CD39 FITC (clone A1)	BioLegend	Cat# 328206; RRID: AB_940425
LYVE-1 AF532 (goat polyclonal, custom conjugate from company)	R&D Systems	Cat# AF2089; RRID: AB_2892756

(*Continued on next page*)

Continued

REAGENT or RESOURCE	SOURCE	IDENTIFIER
CD35 PE (clone E11)	BioLegend	Cat# 333406; RRID: AB_2292231
CD68 AF647 (clone KP1)	Santa Cruz Biotechnology	Cat# sc-20060; RRID: AB_3073741
a-SMA AF488 (clone 1A4)	Thermo Fisher Scientific	Cat# 53-9760-82; RRID: AB_2574461
a-SMA eF660 (clone 1A4)	Thermo Fisher Scientific	Cat# 50-9760-82; RRID: AB_2574362
Lumican AF532 (goat polyclonal, custom conjugate from company)	R&D Systems	Cat# AF2846; RRID: AB_2892757
IRF4 PE (clone IRF4.3E4)	BioLegend	Cat# 646404; RRID: AB_2563005
DC-SIGN AF647 (clone 9E9A8)	BioLegend	Cat# 330112; RRID: AB_1186092
Desmin AF488 (clone Y66)	Abcam	Cat# Ab185033; RRID: AB_2892748
CD49a AF647 (clone TS2/7)	BioLegend	Cat# 328304; RRID: AB_1236407
CD94 AF488 (clone DX22)	BioLegend	Cat# 305506; RRID: AB_314536
Vimentin AF532 (clone O91D3) custom conjugate from company	BioLegend	Cat# NA; RRID: AB_2892753
CD45 PE/iFluor594 (clone F10-89-4)	Caprico Biotechnologies	Cat# 1016185; RRID: 2892742
CD44 AF647 (clone IM7)	BioLegend	Cat# 103018; RRID: AB_493681
BCL2 (clone SP66)	Abcam	Cat# Ab236221; RRID: N/A
Donkey anti-rabbit IgG AF594	Thermo Fisher Scientific	Cat# A-21207; RRID: AB_141637
CD10 (polyclonal)	R&D Systems	Cat# AF1182; RRID: AB_354652
Donkey anti-goat IgG AF680	Thermo Fisher Scientific	Cat# A-21084; RRID: AB_141494
CD21 (clone SP186)	Abcam	Cat# Ab240987; RRID: N/A
Donkey anti-rabbit IgG AF555	Thermo Fisher Scientific	Cat# A-31572; RRID: AB_162543
CD68 iFluor594 (clone KP1)	Caprico Biotechnologies	Cat# 1064135; RRID: 2892745
DC-SIGN (clone h209)	LSBio	Cat# LS-B3782; RRID: AB_10689801
Donkey anti-rat IgG AF647	Jackson ImmunoResearch	Cat# 712-605-153; RRID: AB_2340694
SPARC (polyclonal)	R&D Systems	Cat# AF941; RRID: AB_355728
HI-6B Multiplex Panel - Human CD3, CD4, CD8, FoxP3	Cell IDx	Cat# HI06B-005
CD3 (clone SP7)	Abcam	Cat# Ab16669; RRID: AB_443425
Goat anti-rabbit IgG AF532	Thermo Fisher Scientific	Cat# A-11009; RRID: AB_2534076
PD-1 (polyclonal)	Novus Biologicals	Cat# AF1086; RRID: AB_354588
Donkey anti-goat IgG AF555	Thermo Fisher Scientific	Cat# A-21432; RRID: AB_2535853
Hoechst	Biotium	Cat# 40046; RRID: N/A
IRF4 (clone MUM1p)	Novus Biologicals	NB200-356-0.25 mL; RRID: N/A
Goat anti-mouse IgG1 AF488 (polyclonal)	Thermo Fisher Scientific	Cat# A-21121; RRID: AB_2535764
Donkey anti-rabbit IgG AF647 (polyclonal)	Thermo Fisher Scientific	Cat# A-31573; RRID: AB_2536183
Donkey anti-Goat IgG DL755 (polyclonal)	Thermo Fisher Scientific	Cat# SA5-10091; RRID: AB_2556671
CD21 PE (clone SP186)	Abcam	Cat# ab306325; RRID: N/A
Donkey anti-rat IgG DL 755 (polyclonal)	Thermo Fisher Scientific	Cat# SA5-10031; RRID: AB_2556611
CD4 AF488 (clone EPR6855)	Abcam	Cat# ab196372; RRID: AB_2889191
CD3D AF555 (clone EP4426)	Abcam	Cat# ab208514; RRID: 2728789
CD8 AF647 (clone C8/144B)	Biolegend	Cat# 372906; RRID: AB_2650712
Ki-67 Biotin (polyclonal)	Novus Biologicals	Cat# NB500-170B; RRID: AB_1660247
Streptavidin AF750	Thermo Fisher Scientific	Cat# S21384; RRID: N/A
Desmin AF488 (clone DES/1711)	Novus Biologicals	Cat# NBP2-54503AF488; RRID: N/A
Donkey anti-mouse IgG AF647 (polyclonal)	Thermo Fisher Scientific	Cat# A-31571; RRID: AB_162542
Lumican Biotin (polyclonal)	R&D Systems	Cat# BAF2846; RRID: AB_2139483
Streptavidin AF555	Thermo Fisher Scientific	Cat# S21381; RRID: N/A
Vimentin BL750 (clone O91D3) custom conjugate from company	BioLegend	Cat# N/A; RRID: N/A

(*Continued on next page*)

Continued

REAGENT or RESOURCE	SOURCE	IDENTIFIER
Chemicals, peptides, and recombinant proteins		
Trypan Blue Exclusion	Thermo Fisher Scientific	15250061
Triton X-100	Sigma-Aldrich	Cat# T8787
Tween 20	Millipore Sigma	Cat# 9005-64-5
PBS, pH 7.4	GIBCO	Cat# 10010-023
BD Cytofix/Cytoperm	BD Biosciences	Cat# 554722
Optimal cutting temperature (OCT) compound	Sakura	Cat# 4583
Sucrose	Millipore Sigma	Cat# S0389
Bovine Serum Albumin	Millipore Sigma	Cat# A1933
Human Fc-block	BD Biosciences	Cat# 564219
diH_2O	Quality Biological	Cat# 351-029-101
Fluoromount-G	Southern Biotech	Cat# 0100-01
Hoechst 33342	Thermo Fisher Scientific	Cat# H3570
Lithium borohydride (purchase in 1 g aliquots)	STREM Chemicals	Cat# 93-0397
Chrome Alum Gelatin	Newcomer Supply	Cat# 1033A
AR6 buffer 10X	Akoya Biosciences	Cat# AR600250ML
Bond™ Epitope Retrieval 1-1L	Leica Biosystems	Cat# AR9961
Bond™ Epitope Retrieval 2-1L	Leica Biosystems	Cat# AR9640
Wash Solution 10X Concentrate, 1L	Leica Biosystems	Cat# AR9590
Avidin/Biotin Blocking Buffer	Abcam	Cat# ab64212
Glycerol	Sigma-Aldrich	Cat# G5516-1L
Ethanol, 200 Proof	Decon Labs, Inc.	Cat# 2701
Formalin, 10% neutral buffered	Cancer Diagnostics, Inc.	Cat# FX1003
Xylene, histology grade	Newcomer Supply	Cat# 1446C
ImmEdge Pen	Vector Laboratories	Cat# H-4000
Normal Rabbit Serum	Abcam	Cat# Ab7487
Normal Goat Serum	Abcam	Cat# Ab138478
Critical commercial assays		
Chromium Next GEM Single Cell 5′ Kit v2, 16 rxns	10X Genomics	Cat# PN-1000263
Chromium Next GEM Chip K Single Cell Kit, 48 rxns	10X Genomics	Cat# PN-1000286
Chromium Single Cell Human BCR Amplification Kit, 16 rxns	10X Genomics	Cat# PN-1000253
Library Construction Kit, 16 rxns	10X Genomics	Cat# PN-1000190
AllPrep kit	Qiagen	Cat# 80204
TruSeq Stranded mRNA Library kit	Illumina	Cat# 20020594
Deposited data		
RNA-seq data	This paper	https://doi.org/10.5281/zenodo.6629388
Imaging data	This paper	Data deposited to the Image Data Resource (https://idr.openmicroscopy.org) under accession number idr0158.
ASCT+B Tables	This paper	https://doi.org/10.5281/zenodo.6629388
Software and algorithms		
Leica Application Suite X (LAS X)	Leica Microsystems	RRID: SCR_013673
Imaris and Imaris File Converter (x64, version 9.5.0)	Bitplane	RRID: SCR_007370
Python (version 3.7.0 and higher)	Python	RRID: SCR_008394
SimpleITK Imaris Python Extension	(Radtke et al., 2022)	https://doi.org/10.5281/zenodo.4632320
BostonGene Software	This paper	https://github.com/BostonGene/Cell_Atlas_MxIF

(*Continued on next page*)

Continued

REAGENT or RESOURCE	SOURCE	IDENTIFIER
Fiji	Open source project hosted on GitHub	RRID: SCR_002285
R and RStudio	R Core Team	RRID: SCR_001905
GraphPad Prism, version 10.1.0	GraphPad Software	RRID:SCR_002798
Adobe Photoshop CC 2020	Adobe	
Adobe Illustrator CC 2020	Adobe	
Other		
2-well chambered coverglass	Lab-Tek	Cat#155380
Dissecting mat, flexible, polypropylene	Newcomer Supply	Cat#5218A
Dissecting needles	Newcomer Supply	Cat#5220PL
Histomolds, 15 mm × 15 mm x 5mm	Sakura	Cat#4566
Sterile disposable scalpels #11	Newcomer Supply	Cat#6802A
VWR Superfrost Plus micro slides	VWR	Cat#48311-703
EasyDip slide staining kit	Newcomer Supply	Cat#5300KIT
EasyDip anodized aluminum jar rack holder	Newcomer Supply	Cat#5300JRK
Wash N'Dry coverslip rack	Electron Microscopy Sciences	Cat#70366-16

RESOURCE AVAILABILITY

Lead contact

Further information and requests for resources and reagents should be directed to and will be fulfilled by the lead contact, Andrea Radtke (andrea.radtke@nih.gov).

Materials availability

This study did not generate new unique reagents.

Data and code availability

- The dataset contains the processed scRNA-seq information from human LNs analyzed in this work as a Seurat object. The scRNA-seq information was saved in the rds format for viewing and analysis using the R programming language (to load it in R: scrna_seq_data <- readRDS("scRNA_seq_data_object.rds")). Microscopy data reported in this paper are deposited to the Image Data Resource (https://idr.openmicroscopy.org) under accession number idr0158.
- All original code has been deposited at Zenodo or GitHub and is publicly available as of the date of publication. Accession links are listed in the key resources table.
- Any additional information required to reanalyze the data reported in this paper is available from the lead contact upon request.

EXPERIMENTAL MODEL AND STUDY PARTICIPANT DETAILS

All patients were enrolled on a prospective clonal evolution study for adults with grade I-II or 3A FL who have not received systemic therapy and are without evidence of histologic transformation [NCT03190928]. All patients consented to the trial. The primary endpoint of the study is time to initiation of frontline systemic therapy. The primary objective is to analyze the molecular biology of patients with progression within 2 years of study entry ('early progressors') compared to patients who do not progress and need therapy within 2 years of study entry ('non-progressors'). The secondary objective is to characterize the molecular biology of patients who relapse <2 years after frontline therapy ('early relapsers'). Baseline staging procedures include computed tomography (CT) and fluorodeoxyglucose (FDG)-positron emission tomography (PET) scans along with bone marrow biopsy with aspirate, and patients are staged by the Lugano criteria.[71] All patients are offered excisional LN biopsy, if feasible. Enrolled patients are assigned a baseline FLIPI score[72] and initially assessed by uniform protocol-defined treatment criteria to determine need for immediate frontline therapy. For those who do not meet criteria for treatment, they are monitored with clinic visits every 4 months for 2 years, every 6 months in years 3–5, and then annually until they meet criteria for treatment. CT scans are every 8 months for 2 years, then annually. FDG-PET scans are repeated at 2 years and any time of suspected progression. Normal human mesenteric LNs were obtained from patients undergoing elective risk-reducing gastrectomies or colon resections for colon adenocarcinoma at the National Cancer Institute (NCI) based on an Institutional Review Board (IRB) approved tissue collection protocol (#13C-0076). Biopsies of these LNs were grossly normal as determined by the operative surgeon and histopathologically normal as determined by an expert pathologist. Follicular hyperplasia was identified in one sample (rLN1) based on standard diagnostic evaluation with hematoxylin and eosin (H&E). This

patient sample was included to address inflammation-associated changes versus tumor-induced molecular and morphological alterations in the LN. *BCL2* rearrangements were identified using fluorescence *in situ* hybridization (FISH), the gold standard for translocation detection in lymphoma FFPE.[73] Representative sections from all samples were evaluated using H&E staining before multimodal analysis.

Here, we highlight our ability to profile the TME of patients enrolled onto a prospective clinical trial prior to therapeutic intervention using a multi-modal strategy. This approach required access to an exceedingly rare cohort as well as ample biopsy material. For these reasons, we did not estimate sample size, but did analyze the influence (or association) of sex, age, and race and ethnicity on study results from the larger validation cohort (Figures 8 and S8). We found no association between age but were unable to examine an association between sex and ethnicity due to underpowered data. Samples were assigned to different groups (Non-FL, Non-Progressor, Early Progressor, and Early Relapser) based on clinical criteria for inclusion and exclusion. Clinical group assignments were withheld from the experimental biologists until the final processing of results to blind the study. Spatial biology findings were confirmed using orthogonal methods and alternative imaging platforms. See Table S1 and Figure S1 for clinical and demographic patient details.

METHOD DETAILS

Sample preparation from human tissues

The size of the LNs ranged from less than 1 cm (nLN1 to nLN4), 2 cm (rLN1), to 6 cm (FL1 to FL-28) in diameter. Unfixed LN were measured (L x W x H), cut along the longitudinal axis, and macroscopically inspected. For routine assessment, the LN was sectioned into slices <4 mm in thickness and prepared as FFPE samples as previously described.[74] Depending on the size of the LN, samples were additionally prepared as snap frozen tissue blocks (<5 mm^3) and cell suspensions (at least 20% of total LN volume). All clinical stains were performed with automated immunostainers, BenchMark Ultra (Roche) or BOND-Max (Leica Biosystems), according to the manufacturers' instructions. Diagnostic panels consisted of CD20 (clone L26), CD10 (clone SP67), CD3 (clone 2GV6), BCL2 (clone SP66), BCL6 (clone EP278), Ki-67 (clone MIB-1), CD21 (clone EP3093), CD23 (clone IB12), and IgD (clone 92). See key resources table.

For bulk and scRNA-seq, cell suspensions were prepared by manual disruption of the tissues and frozen down viably. Following tissue homogenization, cells were frozen and stored at −150°C in liquid nitrogen. Prior to sequencing, single cell suspensions were thawed rapidly in a 37°C water bath until ice had just disappeared, then transferred to a 50 mL tube and washed with 50 mL of cold (4°C) 1xPBS. Viable cells were enumerated manually using trypan blue exclusion. For IBEX imaging, human LNs (1 cm^3 or smaller in size) were fixed with BD CytoFix/CytoPerm (BD Biosciences) diluted in PBS (1:4) for 2 days. Following fixation, all tissues were washed briefly (5 min per wash) in PBS and incubated in 30% sucrose for 2 days before embedding in OCT compound (Tissue-Tek) as described previously.[20,21] Non-FL LNs (nLN1, nLN2, rLN1) were only analyzed by scRNA-seq and IBEX imaging. Non-FL LNs (nLN3 and nLN4) and FL samples (FL-1 to FL-28) were prepared as FFPE blocks and imaged using the Cell DIVE-IBEX method. See Table S1 and Figure S1 for more details.

Whole exome sequencing (WES) analysis

Low quality reads were filtered using FilterByTile/BBMap v37.90[75] and aligned to human reference genome GRCh38 (GRCh38.d1.vd1 assembly) using BWA v0.7.17.[76] Duplicate reads were removed using Picard's v2.6.0 MarkDuplicates ("Picard Toolkit", 2019. Broad Institute, GitHub Repository. http://broadinstitute.github.io/picard/; Broad Institute). Indels were realigned by IndelRealigner and recalibrated by BaseRecalibrator and ApplyBQSR using tools taken from GATK v3.8.1.[77] Somatic single nucleotide variations (sSNVs), small insertions, and deletions were all detected using Strelka v2.9.[78]

Bulk RNA-seq processing and analyses

RNA was isolated from cell suspensions using the AllPrep kit (Qiagen) and libraries were generated using the TruSeq Stranded mRNA Library kit (Illumina). Paired end sequencing was performed on an Illumina NextSeq2000. RNA-seq reads were aligned using Kallisto v0.42.4 to GENCODE v23 transcripts 69 with default parameters. The protein-coding transcripts, immunoglobulin heavy, kappa and lambda light chains, and TCR-related transcripts were retained. Noncoding RNA, histone, and mitochondria-related transcripts were removed, resulting in 20,062 protein coding genes. Gene expression was quantified as the sum of the transcripts and re-normalized per million (TPM) and log2-transformed.[79]

Deconvolution of bulk RNA-seq

The Kassandra machine learning algorithm was used to predict cell percentages from bulk RNA-seq.[80] The model consisted of a two-level hierarchical ensemble that used LightGBM as building blocks. The model was trained on artificial RNA-seq mixtures of different cell types (T cells, B cells, NK, macrophages, cancer-associated fibroblasts, and endothelial cells) obtained from multiple datasets of sorted cells. All datasets were isolated from poly-A or total RNA-seq profiled human tissues with read lengths higher than 31 bp and at least 4 million coding read counts. These datasets passed quality control by FASTQC with minimal contamination (<2%). The model was trained to predict the percentage of RNA belonging to specific cell types. Predicted percentages of RNA were later converted

into percentages of cells using the methodology described previously.[81] For Figures 2, 7C, 7D, S7A, and S7B, gene signature scores were calculated using the ssGSEA algorithm from the GSVA R package.[82] Raw scores were medium scaled to (−2, 2) or to (−3, 3) range. See Tables S2, S3, and S4.

scRNA-seq processing and analysis

Viable cells were diluted in 1xPBS such that when loaded on the 10x Genomics Chromium Controller they were at a capture number of ~6,000 cells. After capture, single cell RNA-seq/VDJ libraries were generated using the 10X Chromium Single Cell 5′ gene expression/V(D)J kit and processed according to the manufacturer's instructions. Sequencing of libraries was performed on an Illumina NOVA-Seq and cycling was performed according to the manufacturer's suggestions. All samples had captures performed on the same day with reagents from the same kit. All were sequenced together on multiple sequencing runs to achieve target depth.

FAST-Q files were processed through the 10X Cell Ranger Pipeline v5.0.1 with alignment to a GRCh38 reference (refdata-gex-GRCh38-2020-A for gene expression reads and refdata-cellranger-vdj-GRCh38-alts-ensembl-5.0.0 for TCR and BCR enriched reads). A classical scRNA-seq analysis pipeline was performed as described.[83] The Cell Ranger 4.0 tool and Scanpy 1.9.3 package with Python 3.8 were used.[84] Cells with less than 1,000 unique molecular identifiers (UMIs), more than 10,000 UMIs, and cells with more than 10% mitochondrial gene UMIs were removed. These criteria were empirically selected after initial data analysis in Cell Ranger. These thresholds were applied to minimize several technical clusters (small number of UMIs, high mitochondrial gene expression, and lack of meaningful marker genes). Selection of the top 3,000 over-dispersed genes was performed as described.[85] Next, log-transformation of the data and linear regression of expression data against the number of UMIs and number of genes in cells was performed followed by kNN graph construction. The Leiden algorithm was used for cell clustering with the top 3,000 marker genes and not the whole transcriptome. Elbow plot analysis was used to determine how many PCs were needed to capture the majority of the variation in the data.[86] Data were visualized with UMAP. After overall analysis of all datasets, we selected the subset of T cells, B cells, and other cells and performed an analysis of each subset. Cell types were identified based on marker gene expression. Moreover, cells from the same cell type were selected based on the Leiden clusters and not the UMAP coordinates.

MIXCR v.2.1.7[87] was used to analyze BCR sequences from RNA-seq data. Single clonotypes were grouped into clones with unique VDJ combinations and identical CDR3 nucleotide sequences. B cell clones were further aggregated into clone groups if the VDJ combination was the same and if the CDR3 nucleotide sequences differed no more than 1 nucleotide (Figure S2E).

Gene set enrichment analysis was performed using the C2CP gene set from the mSigDB.[88] Analysis was performed in R v4.1.3 using fgsea v1.20.0.[26] Analysis was performed on a ranked gene set resulting from the log fold change values from differential expression analysis using the FindMarkers function in Seurat v4.1.0.[89] Ribosomal genes were removed before analysis was performed. Plots were generated in ggplot2 v3.3.5.[90] Dot plots were generated using the DotPlot function in Seurat. Gene module scores for individual cells were generated using the AddModule function in Seurat, with the number of control features set to the same length as the gene set of interest. Gene modules were visualized using the VlnPlot function in Seurat. For Figures 2G and 2H, the B cell populations included cycling B, tumor B, GC B, memory B, naive B, and FCRL4$^+$ B single cell clusters.

High content imaging using IBEX

High content imaging was performed on fixed frozen sections as described previously.[20,21] Briefly, 20 μm sections were cut on a CM1950 cryostat (Leica) and adhered to 2 well Chambered Coverglasses (Lab-tek) coated with 15 μL of chrome alum gelatin (Newcomer Supply) per well. Frozen sections were permeabilized, blocked, and stained in PBS containing 0.3% Triton X-100 (Sigma-Aldrich), 1% bovine serum albumin (Sigma-Aldrich), and 1% human Fc block (BD Biosciences). Immunolabeling was performed with the PELCO BioWave Pro 36500-230 microwave equipped with a PELCO SteadyTemp Pro 50062 Thermoelectric Recirculating Chiller (Ted Pella) using a 2-1-2-1-2-1-2-1-2 program. A complete list of antibodies and an IBEX LN antibody panel can be found in Table S6. Cell nuclei were visualized with Hoechst (Biotium) and sections were mounted using Fluoromount G (Southern Biotech). Mounting media was thoroughly removed by washing with PBS after image acquisition and before chemical bleaching of fluorophores. After each staining and imaging cycle, samples were treated for 15 min with 1 mg/mL of $LiBH_4$ (STREM Chemicals) prepared in diH_2O to bleach all fluorophores except Hoechst and Alexa Fluor 594.

MxIF imaging of FFPE tissues

5 μm tissue sections were cut from FFPE samples and placed onto glass slides. Prior to immunolabeling, tissue sections were baked in a 60°C oven for 1 h to adhere the tissues to the slides. Deparaffinization was performed with 2 exchanges of 100% xylene (10 min per exchange) followed by 100% ethanol for 10 min, 95% ethanol for 10 min, 70% ethanol for 5 min, and 10% formalin for 15 min. Antigen retrieval was performed by incubating slides in AR6 buffer (Akoya Biosciences) for 40 min in a 95°C water bath. After 40 min, slides were removed from the water bath and allowed to cool on the bench for 20 min. Blocking and immunolabeling was performed using the PELCO BioWave Pro 36500-230 microwave according to the steps outlined in Table S6. Prior to immunolabeling, tissue sections were outlined with an ImmEdge pen to create a hydrophobic barrier (Vector laboratories) and then rehydrated with PBS. Following a 30-min incubation in blocking buffer, tissue sections were incubated with primary antibodies, washed 3 times in PBS, and then incubated with appropriate secondary antibodies. Directly conjugated primary antibodies were applied last after blocking with 5% normal rabbit and/or goat sera (Abcam). Cell nuclei were visualized with Hoechst (Biotium) and sections were mounted using Fluoromount G (Southern Biotech).

IBEX and MxIF image acquisition and alignment

Representative sections from different tissues were acquired using an inverted Leica TCS SP8 X confocal microscope equipped with 20X (NA 0.75) and 40X objectives (NA 1.3), 4 HyD and 1 PMT detectors, a white light laser that produces a continuous spectral output between 470 and 670 nm as well as 405, 685, and 730 nm lasers. Panels consisted of antibodies conjugated to the following fluorophores and dyes: Hoechst, Alexa Fluor (AF)488, AF532, phycoerythrin (PE), PE/iFluor594, eF570, AF555, AF594, iFluor (iF)594, AF647, eF660, AF680, and AF700. All images were captured at an 8-bit depth, with a line average of 3, and 1024x1024 format with the following pixel dimensions: x (0.284 μm, 40X), y (0.284 μm, 40X), x (0.568 μm, 20X), y (0.568 μm, 20X), and z (1 μm). Images were tiled and merged using the LAS X Navigator software (LAS X 3.5.5.19976). For IBEX tissue imaging, multiple tissue sections were examined before selecting a representative tissue section that contained several distinct follicles, often resulting in unusually shaped region of interests. For multiplexed imaging of FFPE tissue sections, whole tissue sections were imaged using a 20X objective. To ensure proper alignment over distinct imaging cycles, careful attention was paid to the quality of image stitching achieved with the Leica software and z-stacks were set by manual inspection of notable features such as unusually shaped nuclei throughout the tissue volume. These unusual features were matched across the z stack and over multiple cycles of IBEX as outlined in a detailed protocol.[21] Fluorophore emission was collected on separate detectors with sequential laser excitation of compatible fluorophores (3–4 per sequential) used to minimize spectral spillover. The Channel Dye Separation module within the LAS X 3.5.5.19976 (Leica) was then used to correct for any residual spillover. For publication quality images, Gaussian filters, brightness/contrast adjustments, and channel masks were applied uniformly to all images. Image alignment of all IBEX panels was performed as described previously[20,21] using SimpleITK.[91,92] Software can be downloaded via a zip file from the Imaris extensions code repository (https://github.com/niaid/imaris_extensions/archive/refs/heads/main.zip). Installation instructions are available online: [https://github.com/niaid/imaris_extensions] and in the README.md file which is part of the zip file. Additional details can be found in the XTRegisterSameChannel SimpleITK Imaris Python Extension YouTube tutorial (https://youtu.be/rrCajI8jroE). Please see sample data on Zenodo for usage of the software [https://doi.org/10.5281/zenodo.4632320].

To obtain multiplexed images of FFPE tissue sections, serial sections were imaged with 4 distinct panels of antibodies containing Hoechst and 2–8 antibodies per panel (Table S6). Following image acquisition, images were aligned using Hoechst as a fiducial. As a first approximation, a pathologist manually obtained rotation matrices for cell-cell alignment across serial sections using downsampled Hoechst channels and GIMP (GNU Image Manipulation Program) image editor. Following image rotation for alignment, the register_translation function from the skimage python package was used to find a translation vector. Upon identification of a suitable rotation matrix and translation vector based on Hoechst^{+} nuclei, these parameters were applied to all serial image stacks. The register_translation function uses cross-correlation in Fourier space, optionally employing an upsampled matrix-multiplication DFT (Discrete Fourier transform) to achieve arbitrary subpixel precision.[93] Artifacts (such as fluorophore aggregates and uneven staining) were manually masked by 3 pathologists.

Object-based segmentation of IBEX images

Object-based cellular segmentation was performed using a convolutional neural network (CNN)-based approach with Mask R-CNN architecture and ResNet-50 as a backbone.[94] As an input three channels were used: Hoechst for nuclei, CD45 as a base membrane, and composite of several other membrane markers (CD138, CD163, CD94, CD69, CD8, CD4). Composite images were made by choosing the brightest pixel across all marker channels for each separate pixel position. Final images were normalized to a range of 0–1 by dividing by the maximal possible intensity value (255). The prediction window size was set to 256 pixels on each side. To stitch prediction tiles, the original images were cropped into intersecting windows with 136 pixel steps. A 60 pixel buffer was used on every side of prediction window (256 - 60 * 2) for predicted cell selection in overlapping areas. Buffer size was chosen as a half of a maximum potentially possible cell side size. The training settings for the deep learning algorithms used in this work are given in Table S5.

Cell typing of IBEX images

Among the 39 antibodies included in the multiplexed imaging panels, three distinct staining patterns were observed: membrane or cytoplasmic (all markers except for BCL6, Ki-67, FOXP3, IRF4, CD68), nuclear (BCL6, Ki-67, FOXP3, IRF4), and endosomal/lysosomal (CD68). The CNNs were trained to recognize the presence or absence of a biomarker based on these patterns of expression for individual cells. The input image consisted of three channels: Hoechst, marker of interest, and segment mask for a cell of interest. Input images were cropped to 128x128 pixels, corresponding to the cell bounding box and its nearest environment, and normalized to values ranging from 0 to 1, dividing by the maximal possible intensity value. All three networks had the same architecture (ResNet-50) with two neurons in the last layer (signal present/signal absent) with Softmax activation function in the output layer. The Softmax activation function allows normalization of the CNN's output to values from 0 to 1, where 1 corresponds to positive expression, 0 corresponds to negative expression of a given marker, and 0.5 corresponds to an uncertain prediction (hard case for NN, outcomes have equal weights). This approach is also sensitive to the spatial distribution of each specific marker. Every possible ground truth cell type can be expressed as a sequence of markers that must be present (encoded as 1), may be present (creating two versions of this cell type, with 0 and 1) and must be absent (encoded as 0). For example, a particular cell may be defined as a B cell if this cell is CD20^{+} (encoded as 1), CD21$^{+/-}$ (encoded as 1 or 0), and CD3^{-} (encoded as 0)). Cosine similarity is calculated between every sequence of cell expression and every cell type encoding vector. The final cell type is defined as the closest match based on probability. Cell annotations and counts across samples can be found in Table S2.

Tessellation masks for imaging data

Masks for certain immune, myeloid, and stromal markers were generated by Otsu's method.[95] The following markers were masked for IBEX images: CD11c, CD21, CD23, CD31, CD35, CD39, CD49a, CD68, CD163, CXCL13, Collagen IV, DC-SIGN, Desmin, Lumican, LYVE-1, SPARC, α-SMA, and Vimentin. The following markers were masked for MxIF images: CD3, CD8, CD20, CD21, CD68, DC-SIGN, Desmin, Lumican, PD-1, SPARC, and α-SMA. CD4 T cells were defined as $CD3^{+}CD8^{-}$ due to an inability to detect CD4 in the experimental conditions described for MxIF images. All markers, except for PD-1, were evaluated in a larger cohort using Cell DIVE-IBEX. The following markers were masked for Cell DIVE-IBEX images: BCL2, CD3, CD4, CD8, CD10, CD20, CD21, CD68, DC-SIGN, Desmin, IRF4, Ki-67, Lumican, α-SMA, SPARC, and Vimentin. All channel masks were inspected by pathologists and compared to the raw immunofluorescence signal. In a few select instances of poor algorithm performance, thresholds were manually corrected using Fiji.[96] We define a tessellation as a process of splitting a mask derived from a marker of interest into non-intersecting squares that covers a full image area. A signal density heatmap is then created by computing the percentage of positive pixels in each of these squares. Every square can be roughly considered as a ''pseudo-cell'' measuring 16x16 pixels for stromal and myeloid subpopulations identified in IBEX images. Percentages of masks in each square ''pseudo-cell'' is equivalent to mean cell marker expression for object-based cellular segmentation.

For phenotyping stromal cells from IBEX imaging data, tessellation-based analysis was performed with over a dozen markers (CD21, CD23, CD31, CD35, CD39, CD49a, CXCL13, Collagen IV, Desmin, Lumican, LYVE-1, SPARC, α-SMA, and Vimentin), including several markers not exclusive to stromal cells, e.g., CD39, CD49a, SPARC). For markers expressed by stromal and non-stromal elements, e.g., CD39 on Tregs, stromal masks were first created to mark an area of interest based on co-localization with lineage-defining markers, e.g., CD31 for endothelial cells and vimentin for mesenchymal cells. For well-described stromal markers (CD31, LYVE-1, CD21, Desmin, Vimentin, Lumican), tessellation masks were created directly from the channel data and thresholded by 0.2, an empirically derived parameter. To elaborate, this limit (0.2) corresponded to the value where the amount of 'masked pixels' and 'empty pixels' were equal and intersected on an x-y plot with the 'mask threshold' on the x axis and 'fraction of pixels covered by mask' on the y axis (Figure S3D). Clustering was then performed on masked pixel data using the unsupervised clustering algorithm Phenograph[97] with cosine distance metric and 30 nearest neighbors. For phenotyping myeloid cells from IBEX imaging data, a similar approach was implemented using 5 markers (CD11c, CD163, CD68, DC-SIGN, and SPARC) where only the SPARC marker was not exclusive to macrophages and dendritic cells. Although CD1c and HLA-DR were detected on myeloid cell subtypes, these markers are also expressed on B cell subpopulations. Due to contaminating signal from B cells, the dominant population in FL samples, CD1c and HLA-DR were excluded from myeloid cell phenotyping. For CD68 and CD163 markers, the tessellated mask was an integration of pixel-level data and corresponding macrophage segment masks. To exclude empty tessellation squares, we filtered empty squares by a 0.1 threshold. A different masking strategy was applied for myeloid cells in order to detect the pseudopodia of these cell types which typically cover less area than stroma. K-Means was used as a clustering algorithm. These tessellation-based approaches were also used to define cellular communities present in both IBEX and MxIF images using 100 and 50 pixel-sized squares (Figure S6C), respectively. For these analyses we used 11 markers and the K-Means clustering algorithm. A similar workflow was applied to the Cell DIVE-IBEX images using 20 pixel-sized squares and the markers included in the immune and stromal panels (Figures 8, S8, and Table S6). Cell annotations and counts across samples can be found in Table S2.

Assessment of image analysis workflows

The precision and recall of our Mask region-convolutional neural network (R-CNN) workflow was compared to DeepCell[98] and StarDist,[99] two widely used neural network-based segmentation algorithms. Validation of the trained cell segmentation model showed high accuracy (0.80 F1-score), demonstrating superior performance compared to other methods (DeepCell and StarDist - 0.55 and 0.78 F1-score, respectively). The pathologist-determined accuracy (0.84 mean F1-score) indicated a near-human performance of the developed method.[100] To evaluate the accuracy of our cell typing model, we compared the concordance between our algorithm and manual annotations by 3 pathologists for 200 cells randomly sampled from each IBEX dataset. This workflow required the evaluation of combinations of 39 protein markers present in the IBEX images. Normalized expression values obtained from the cell typing model allowed automated cell recognition, reporting 72–79% concordance between annotators and the algorithm.

Follicles shape analysis

To compare the follicle shape across small and large ROIs acquired using distinct imaging methods and sample preparations (IBEX/fixed frozen versus MxIF/FFPE), masks were applied to B cell follicles and sample parameters were calculated. B cell follicle masks from IBEX images were obtained by manual annotation from pathologists based on concentrated areas positive for CD20 and CD21 and reduced lumican signal for most samples (Figure S5A). Follicle masks were created based on CD21 and CD20 signal alone for MxIF images. Once masks were generated, the area, minimal distance to the nearest follicle, elongation, and compactness were calculated for each follicle. As a final step agglomerative clustering with ward linkage was performed on given follicle shape parameters.[101] The following elongation formula was used:

$$\frac{m_{1,1}+m_{2,2}+\sqrt{(m_{1,1}-m_{2,2})^2+4m_{1,2}^2}}{m_{1,1}+m_{2,2}-\sqrt{(m_{1,1}-m_{2,2})^2+4m_{1,2}^2}}$$

Compactness formula where A and P stand for area and perimeter correspondingly: $\frac{4\pi A}{P^2}$. We extended our follicle analysis to a larger cohort (n = 29). By analyzing 4.5 times more follicles, we were able to construct a comprehensive examination of the follicular growth pattern of FL, resulting in 5 different clusters based on 6 distinct parameters. For the Cell DIVE-IBEX images (Figures 8 and S8), the following parameters were calculated as described before: area, minimal distance to the nearest follicle, elongation, and compactness. Solidity was determined as the ratio of the follicle area to the convex hull area. Area, perimeter, convex hull area, and minimal distance between follicles were calculated using the Shapely Python package (Version 2.0.1).

Community analysis of IBEX images

To perform community analysis, a cell neighborhood graph was generated with Delaunay triangulation algorithm from SciPy spatial algorithms package using coordinates derived from cell centroids.[102] In this graph, each cell is represented as a node, and adjacent cells are connected via edges. To remove outlier edges, we aggregated lengths of all edges for all cells in the dataset across all samples, and a threshold value was selected as the 95th percentile of all lengths – 28.4 μm, edges longer than this threshold were removed. After this operation, we assigned features for every node in the graph, which used this model: 1) cell type assigned as categorically encoded vector, 2) percentages of selected binary masks in 56.8 μm radii underneath this cell, 3) median distance of edges connected to this node. Using this graph, an Adversarially Regularized Variational Graph Auto-Encoder[103,104] was trained to obtain short descriptive vector representation of cell neighborhoods in an unsupervised, generative-adversarial manner. The framework consists of two models: a variational graph autoencoder and an adversarial model (3 layered perceptron). The latter model is used for regularization of the main graph autoencoder model. During training, the autoencoder learns to correctly predict node edges and reject randomly added non present edges. In parallel the discriminator model is trained to distinguish between learned autoencoder representations and their random permutations, thus regularizing the model to closely follow the latent data distribution, since the autoencoder is rewarded for correct generation of data, close to the real distribution. Thus, in the process of training, an autoencoder model learns representation of tissue topology, since it can reconstruct correct contacts for a given cell and has learned representations that closely follow the true data distribution. These representations, or embeddings, learned by the autoencoder, allow clustering and detection of cell similarities by topological features of the given tissue.

The model was trained for a fixed number of epochs (100) and the model with lowest loss was selected for downstream analysis. The trained autoencoder predicted embedding vectors for all samples in the cohort and these vectors were then clustered using the K-means algorithm to obtain 15 different clusters, which represent neighborhoods of cells or communities. To facilitate community description, the mean cell composition and mean mask percentages were calculated for each community. Communities were grouped based on the dominant cell type and morphological structures present in them: B- and T-cells enriched neighborhoods, myeloid- and stroma-enriched neighborhoods. Communities were visualized by drawing cell contours and coloring them according to community type. A detailed description of IBEX communities (Figure 5) and comparison with MxIF communities (Figure 6) can be found in Table S2. The training settings for the deep learning algorithms used in this work are given in Table S5.

Slide concordance analysis

Tessellation-based communities were used to analyze the concordance of small IBEX ROIs with large, full tissue section ROIs from MxIF. For each sample, we performed sampling with window side sizes varying from 2,500 to 17,000 pixels (2.02–98.8 mm^2) with 500 pixel steps (284 μm). Crops were sampled uniformly, with distances between centers equaling 200, 300, 400, and 500 pixels for sides of 2500–4000, 4500–6000, 6500–8500, and 10000–17000 pixels correspondingly. Crops with a tissue area of less than 50% were excluded from further analysis. We then measured the Pearson correlation between the percentage of tessellation communities for given crops and the full slide.

Number of cells to be sequenced

For Figure 7B, we predict the number of cells that need to be profiled by scRNA-seq based on frequencies obtained from IBEX imaging data. Cell numbers were calculated based on cell frequencies obtained from the entire $1.8x10^6$ cell IBEX dataset. A cluster size of 50 cells was used to estimate the number of cells to be sequenced.

Correlations between single cell communities

For Figure 7A, percentages for B cells, $CD4^+$ T cells, and $CD8^+$ T cells are compared between IBEX segmentation, scRNA-seq cell typing, and Kassandra reconstruction. Myeloid cells are compared between Kassandra reconstruction from bulk RNA-seq data and IBEX tessellation squares normalized by area of tissue imaged. Stromal cells are derived from IBEX tessellation squares normalized by area. Statistical analysis is reported in Table S7. For Figures 7C, 7D, S7A, and S7B, fibroblast and cytokine gene signatures were manually curated from the literature (Table S8).[35,45,47,105,106] Pairwise correlations were performed between RNA-seq gene signatures, described in deconvolution of bulk RNA-seq, and IBEX communities, described in community analysis of IBEX images.

Cell DIVE-IBEX imaging of FFPE tissues

Deparaffinization and antigen retrieval were performed using a Leica Bond RX (Leica Biosystems). A dual antigen retrieval approach consisting of 30 min with Epitope Retrieval Solution 1 and then 30 min with Epitope Retrieval Solution 2 was determined to give the best immunolabeling results.[107] Slides were labeled with Hoechst (Biotium) and mounted with a 50:50 mixture of Glycerol

(Sigma-Aldrich) and PBS. Whole slide images were acquired using the Cell DIVE[22] imaging system equipped with a 20X (NA 0.75) objective, (Leica Microsystems, Wetzlar, Germany). Slides were placed into ClickWell slide holders (Leica Microsystems, Wetzlar, Germany) and calibration scans were performed as outlined in the Leica Microsystems Cell DIVE software (Version 4.0). Additionally, autofluorescence (AF) images were captured and used to automatically subtract the background from each image. Serial sections were labeled with the immune and stromal panel (Table S6) using the PELCO BioWave Pro 36500-230 microwave. Panels consisted of the following IBEX compatible fluorophores: Hoechst, AF488, AF555, PE, AF647, DL755, AF750, and BL750 (Table S6). Following image acquisition, slides were removed from the ClickWell slide holders, washed thoroughly to remove mounting media, and incubated with 3 exchanges of 1 mg/mL $LiBH_4$, 15 min per incubation, to completely extinguish fluorescence for a total time of 45 min. Slides were washed thoroughly in PBS, labeled with antibodies for the next imaging cycle, loaded into ClickWell slide holders, mounted with 50:50 Glycerol:PBS, and then imaged using the Cell DIVE. The following image processing steps were performed by the Cell DIVE imaging software: mosaic merge of individual tiles, registration of images using a repeated marker (Hoechst labeled nuclei), autofluorescence subtraction, and illumination correction.[108] The raw individual channel tif files created by the Cell DIVE were combined into a multi-channel Imaris file using the open source tif2ims software available on GitHub (https://github.com/zivy/tif2ims). Artifacts (such as fluorophore aggregates and corrupted pixels) were manually masked by 3 pathologists. For Figures S8I and S8J, fibroblast includes fibroblastic reticular cells (FRCs)[32,109] and other subtypes (myofibroblasts, smooth muscle cells, cancer-associated fibroblasts[110]). SPARC is expressed by fibroblasts, endothelial cells, macrophages, and involved in cell-matrix interactions.[51] Vimentin is expressed by fibroblasts and activated macrophages.[109–111]

Linear model identifying early relapsers

Data from the immune and stromal communities were used to create generalized linear models (GLM) for the validation cohort samples. The models were created using a binary output comparing the other FL groups (early progressors or non-progressors) to the early relapsers. Due to low sampling size, sex, age, and ethnicity were not included in the models. There was no significant difference in age between the groups. To determine the communities that best separated the early relapsers from the other FL patients, we created a linear model using every possible combination of the 16 communities. Outputs for the models were saved to determine the number of times a community appeared in a significant model determined by the intercept p value being <0.1. The top three communities appearing in significant models were then used to create a GLM. This model was applied to each patient sample and the output was compared. The models were generated in R v4.1.3 using the stats package (v3.6.2).

QUANTIFICATION AND STATISTICAL ANALYSIS

Statistical analysis was performed using Prism (GraphPad Version 9.4.1) and R v4.1.3 using fgsea v1.20.0. Statistical details can be found in the figures and results. For all data, individual n representing cells or tissue sections from a patient sample are plotted with the mean ± SEM shown. For comparisons in Figure 7A, an ANOVA with Tukey's multiple comparison test was performed with significance defined using reported p values (Table S7). For Figures 8 and S8, an ANOVA was used (Kruskal-Wallis test) that did not assume a Gaussian distribution. Multiple comparison tests were performed to analyze the data between the groups. A Benjamini-Hochberg method for false discovery rate (FDR) p value correction was used to correct p values for multiple comparisons. A cutoff of 0.1 was used for significance. Due to several factors outlined here, it is challenging to recruit sufficient numbers of patients with adequate tissue biopsies. For these reasons, we did not estimate the sample size or exclude any data or subjects. Samples were assigned to groups based on clinical records.

ADDITIONAL RESOURCES

A complete list of antibodies, including positive and negative results, protocols, datasets, and software are shared in the IBEX Imaging Community.[107] The complete IBEX panel and accompanying antibody validation reports are available through the Human Reference Atlas portal (OMAP-1) (https://humanatlas.io/omap).[50]